Fluid inclusion and H–O–C isotope geochemistry of the Yaochong porphyry Mo deposit in Dabie Shan, China: a case study of porphyry systems in continental collision orogens

Pin Wang, Yan-Jing Chen, Bin Fu, Yong-Fei Yang, Mei Mi & Zhong-Lie Li

International Journal of Earth Sciences
GR Geologische Rundschau

ISSN 1437-3254

Int J Earth Sci (Geol Rundsch)
DOI 10.1007/s00531-013-0982-5

Springer

Int J Earth Sci (Geol Rundsch)
DOI 10.1007/s00531-013-0982-5

ORIGINAL PAPER

Fluid inclusion and H–O–C isotope geochemistry of the Yaochong porphyry Mo deposit in Dabie Shan, China: a case study of porphyry systems in continental collision orogens

Pin Wang · Yan-Jing Chen · Bin Fu · Yong-Fei Yang · Mei Mi · Zhong-Lie Li

Received: 14 July 2013 / Accepted: 11 November 2013

Abstract The Yaochong porphyry Mo deposit in Xinxian County, Henan Province, China, is located in the Hong'an terrane, that is, the western part of the Dabie orogen. The Dabie orogen is part of a >1,500 km long, Triassic continental collision belt between the North China Block and the South China Block. Four types of vein are present. Paragenetically, from early to late, they are as follows: stage 1 quartz + K-feldspar ± pyrite ± magnetite vein; stage 2 quartz + K-feldspar + molybdenite ± pyrite vein; stage 3 quartz + polymetallic sulfides ± K-feldspar vein; and stage 4 quartz ± carbonate ± fluorite vein. Four compositional types of fluid inclusion, pure CO_2, CO_2 bearing, aqueous, and solid bearing, are present in quartz from the first three stages; only low-salinity aqueous fluid inclusions occur in quartz from the last stage. All the estimated salinities are ≤13.1 wt% NaCl eq., and no halite crystals were identified. Homogenization temperatures for the fluid inclusions from stages 1 to 4 are in the ranges of 262–501, 202–380, 168–345, and 128–286 °C, respectively, and estimated depths decrease from 6.9 to 8.9 km, through 6.2–7.2, to ~4.7 km. Quartz separates from the veins yielded a $\delta^{18}O$ value of 7.7–11.2 ‰, corresponding to $\delta^{18}O_{H2O}$ values of −1.3 to 6.9 ‰ using temperature estimates from fluid inclusion data; δD_{H2O} values of fluid inclusion vary from −80 to −55 ‰, and $\delta^{13}C_{CO2}$ from −2.3 to 2.7 ‰, suggesting that the ore-fluids evolved from magmatic to meteoric sources. We conclude that the ore-forming fluid system at Yaochong was initially high temperature, high salinity, and CO_2-rich and then progressively evolved to CO_2-poor, lower salinity, and lower temperature, by mixing with meteoric water, which results in ore precipitation.

Keywords Porphyry Mo deposit · Fluid inclusions · Stable isotopes · CO_2-rich high-salinity fluid · Dabie Shan · Continental collision orogen

Introduction

Porphyry-type deposits are significant repositories of copper, gold, and molybdenum. They are most commonly discovered in continental and oceanic magmatic arcs, such as the southwestern Pacific Islands and the Andes (Sillitoe 1972; Pirajno 2009). For decades, the characteristics, genetic models, and tectonic settings of porphyry Mo deposits, especially in the Cordillera, western North America, have been extensively studied and well documented (Clark 1972; Wallace et al. 1978; Woodcock and Hollister 1978; Sillitoe 1980; Mutschler et al. 1981; Westra and Keith 1981; Carten et al. 1993; Mirsa 2000; Seedorff and Einaudi 2004a, b; Seedorff et al. 2005; Klemm et al. 2008; Ludington and Plumlee 2009). Recently, continental collision belts have been also proven to be favorable for porphyry-type Mo mineralization

P. Wang · M. Mi
Key Laboratory of Mineralogy and Metallogeny, Guangzhou Institute of Geochemistry, Chinese Academy of Sciences, Guangzhou 510640, China

Y.-J. Chen (✉) · Y.-F. Yang
Key Laboratory of Orogen and Crust Evolution, Peking University, Beijing 100871, China
e-mail: yjchen@pku.edu.cn; gigyjchen@126.com

B. Fu
Research School of Earth Sciences, Australia National University, Canberra, ACT 2000, Australia

Z.-L. Li
Henan Bureau of Geological Exploration for Non-Ferrous Metals, Zhengzhou 450052, China

Published online: 01 December 2013

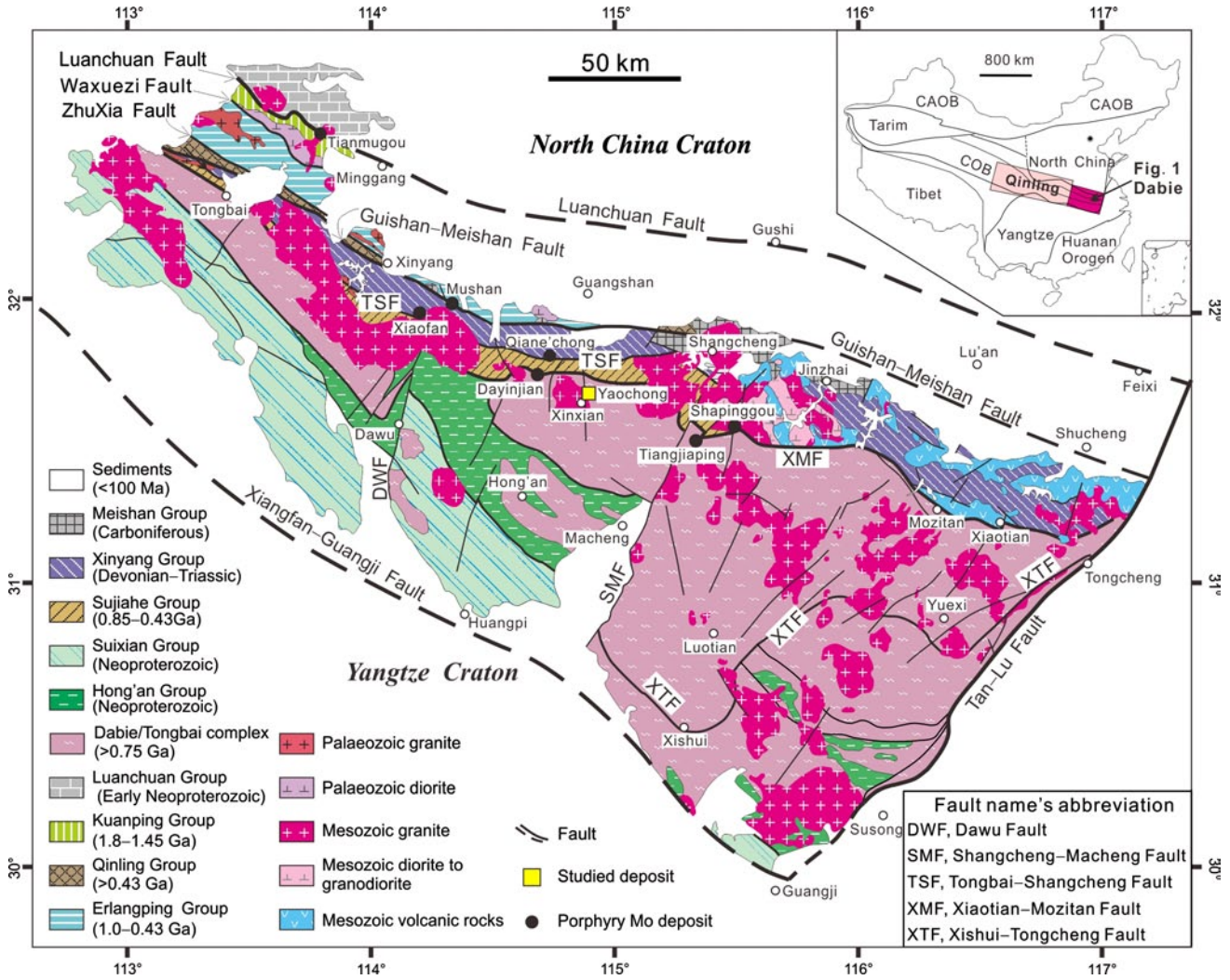

Fig. 1 Sketch map showing the geology of the Dabie Shan and the locality of the Yaochong Mo deposit (Modified after Chen and Wang 2011; Liu et al. 2004, 2013). *CAOB* Central Asia Orogenic Belt, *COB* Central Orogenic Belt

(Chen and Fu 1992; Richards 2009; Pirajno 2013; Chen 2013 and references therein), such as the Qinling orogen (e.g., Chen et al. 2000, 2007a; Li et al. 2007, 2013a; Mao et al. 2008; Zhang et al. 2011a, b; Yang et al. 2012, 2013a) and the Central Asia Orogenic Belt (Xiao et al. 2009; Zeng et al. 2011, 2013; Wu et al. 2013; Xiang et al. 2013; Zhang et al. 2013a; Chen et al. 2009, 2012 and references therein).

The Qinling–Dabie orogenic belt is a Mesozoic continental collision belt, suturing the North China Craton and the Yangtze Craton (Fig. 1). The western part of this orogenic belt, Qinling Orogen, hosting six giant Mo deposits (each with a reserve of >0.5 Mt Mo) and dozens of large (0.1–0.5 Mt Mo) and medium (0.01–0.1 Mt Mo) deposits, is considered to be one of the most economically important Mo provinces in the world (e.g., Chen et al. 2007a, 2009; Li et al. 2007). While the eastern part of the orogenic belt, Dabie Shan, had been regarded as a barren area for a long time, because no important deposit had been discovered in last century (Chen and Wang 2011 and references therein), it is widely developed with ultrahigh-pressure (UHP) metamorphic rocks which have drawn much attentions of geologists (e.g., Wang et al. 1989; Xu et al. 1992; Ames et al. 1993; Chavagnac and Jahn 1996; Liu et al. 2004, 2008, 2013; Zheng et al. 2006; Jahn and Chen 2007). Recently, the discoveries of large to giant porphyry Mo deposits at Tangjiaping in 2004, Qian'echong in 2007, and Shapinggou in 2008 in Dabie Shan (Fig. 1; Wang et al. 2009; Chen and Wang 2011; Chen et al. 2013; Li et al. 2013b; Yang et al. 2013b) show that the UHP metamorphic terrane is still potential for ore exploration. Nevertheless, the origin of the porphyry Mo system in Dabie Shan and its relationship with granitoids and UHP metamorphic rocks remain open.

The Yaochong porphyry Mo deposit in Xinxian County, Henan Province, was first discovered in 2008 by the Henan Bureau of Geological Exploration for Non-ferrous metals, with a proven reserve of >50,000 t Mo in metal (Wang et al. 2013). In this contribution, we present the research results of fluid inclusions (FIs) and stable isotopes, decipher the evolution of the ore-forming fluids at the Yaochong porphyry Mo deposit, and consequently, establish a genetic model for the porphyry Mo deposits in continental collision belts.

Regional geology

The Dabie Shan is the eastern part of the E-trending Central Orogenic Belt (COB) which is well known as a Mesozoic continental collision orogen. It is bounded by the Luanchuan Fault (Gushi Fault) to the north and the Xiangfan–Guangji Fault to the south (Fig. 1). The NW-trending Guishan–Meishan fault is considered as the final suture zone between the North China and Yangtze continental blocks (Hu 1988; Chen and Fu 1992; Chen and Wang 2011).

To the north of Guishan–Meishan fault, the Kuanping Group (Mesoproterozoic), the Erlangping Group (Neoproterozoic–Early Paleozoic), and the Qinling Group (mainly Paleoproterozoic) are well developed from north to south and both compose the Caledonian metamorphic accretion belt of the North China Craton. This Caledonian metamorphic accretion belt is locally overlain by Late Paleozoic strata, e.g., the Carboniferous Meishan Group, a sedimentary succession of mudstones, sandstones, and calcareous shales (Yang 2007). To the south of the Guishan–Meishan fault, five lithotectonic units are identified (Fig. 1; Liu et al. 2004). From north to south, they are (1) Xinyang Group, (2) Sujiahe Group, (3) Dabie or Tongbai metamorphic complex containing UHP (ultra-high-pressure) rocks, (4) Hong'an Group, and (5) Suixian Group. The Xinyang Group is a suturing mélange composed of Devonian–Triassic strata and occasional ophiolite segments and blocks sliced from the Qinling Group (Hu 1988; Yin et al. 1991; Zhang et al. 2011a, 2013b). It is subdivided into the Guishan and Nanwan formations in ascending sequence, with lithologies being dominated by volcanic and sedimentary rocks, respectively (Henan Bureau of Geology and Mineral Resources 1989). The Guishan Formation is a mixture of the segments from Qinling Group, mafic to felsic volcanic rocks containing ophiolite slices, and forearc sediments comprising fine-grained clastic sedimentary rocks with minor marble intercalations (Liu et al. 2013). The Nanwan Formation is composed of bedded quartzose sandstones, pelites, and minor graywackes (Ye et al. 1993) deposited on a newly accreted complex (Liu et al. 2013). The Neoproterozoic–Early Paleozoic Sujiahe Group (also called Xiaojiamiao Formation) consists of the Balifan mélange that comprises highly strained granites, mylonitized quartzofeldspathic gneisses, epidote-amphibolites, and strongly elongated metagabbro bodies, and the Huwan HP unit composed of mylonitized granites, quartzofeldspathic gneisses, mica schists, marbles, and eclogite enclaves (Liu et al. 2008). The Dabie (or Tongbai) metamorphic complex, accommodating UHP eclogite massifs, consists of high-grade metamorphosed Neoproterozoic tonalitic–trondhjemitic–granodiorite (TTG) gneisses and subordinate migmatites (Bryant et al. 2004; Hacker et al. 1998, 2000; Jahn et al. 1999; Zheng et al. 2005, 2006) and Archaean to Proterozoic supracrustal rocks including granulites, amphibolites, biotite–plagioclase gneisses, and marbles. The complex was intruded by voluminous Mesozoic granitic intrusions (Zheng et al. 1998, 2006). The Hong'an Group (Neoproterozoic) is lithologically dominant of quartzofeldspathic schists, muscovite–albite, and two-mica gneisses, with minor eclogites, amphibolites, marbles, metaphosphorite layers, and graphite schist (Liu et al. 2004, 2008). The Suixian Group is a low- to middle-grade metamorphosed Neoproterozoic volcanic-sedimentary sequence, containing voluminous blueschists and also called the Mulanshan blueschist unit (Liu et al. 2004, 2008).

The above-mentioned NW-trending strata and faults are usually crosscut by NE- to NNE-striking faults developed since the Jurassic, resulting in a latticed-style fault system that controls the development of the Cretaceous intrusions and related mineralization. The Dabie Shan is displaced into Tongbai, Western Dabie Shan, and Eastern Dabie Shan from west to east, with the Dawu and the Shangcheng–Macheng faults being the boundaries (Fig. 1).

Magmatism in Dabie Shan mainly occurred in the Early Cretaceous, including granitic intrusions, minor diorite-granodiorite, and volcanic rocks (Fig. 1). The Cretaceous granitoids were formed in an extensional, post-orogenic environment (Zhong et al. 1999; Hacker et al. 2000; Suo et al. 2000; Xu et al. 2007; Zhao et al. 2007), and they mainly intruded into the Dabie metamorphic complex, occurring in the southeast of the Dabie Shan. The Cretaceous granitoids are widely distributed along the NW- and NNE-trending faults or in their intersections and comprise deeply seated granite batholiths and small stocks. The small Cretaceous granitic stocks are often associated with porphyry-type Mo mineralization, such as Xiaofan, Mushan, Dayinjian, Tangjiaping, Qian'echong, and Shapinggou (Fig. 1), thereby constituting the Dabie Mo belt (Chen and Wang 2011; Mao et al. 2011; Li et al. 2013b).

Deposit geology

The Yaochong Mo deposit is located in the Dabie metamorphic complex (Fig. 2) which in this area includes

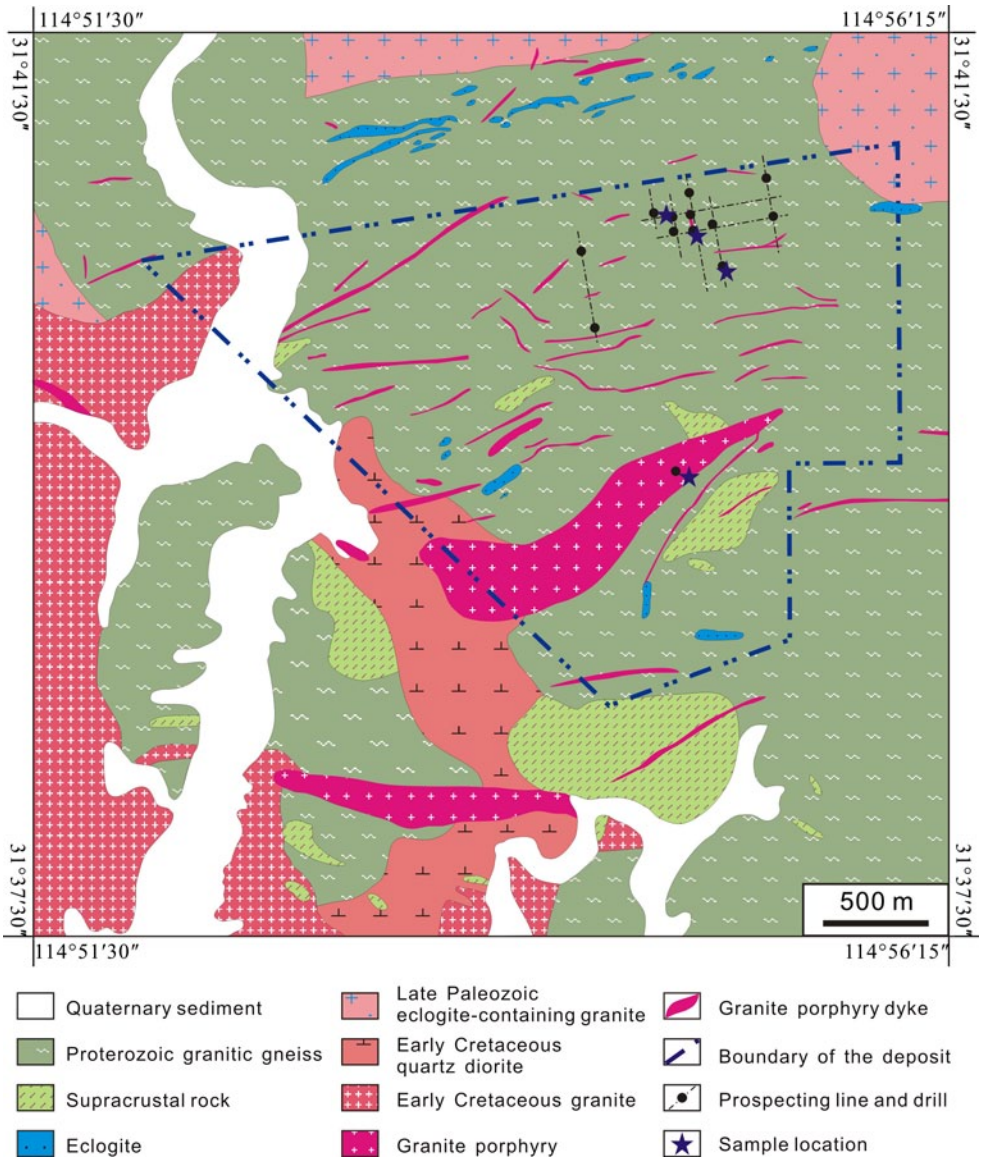

Fig. 2 Geological map of the Yaochong Mo deposit, showing the location of sampled drill sites

Neoproterozoic granitic gneisses and supracrustal rocks. The Neoproterozoic granitic gneisses are widespread in the region, and include tonalitic, granodioritic, and monzogranitic gneisses, whereas the supracrustal rocks occur as enclaves, lithologies of which are biotite gneisses, eclogites, plagioclase gneisses, plagioclase amphibolites, muscovite–quartz schists, and biotite schists.

Phanerozoic magmatism mainly took place during the Late Paleozoic and the Early Cretaceous (Fig. 2). The Late Paleozoic plutonic rocks intruded the Neoproterozoic granitic gneisses, outcropping in the north of the deposit, and the contact zone was partly altered by later deformation. The main Late Paleozoic intrusions are gneissoid fine-grained eclogite-containing granite, with magnetite as accessory mineral. The Early Cretaceous intrusions consist of quartz diorite, fine- or medium-grained monzonitic granite, porphyry stocks and dykes, typically with complicated patterns, and multistage intrusions (Fig. 2). Diorite or plagioclase amphibolite enclaves can be observed in the quartz diorite and monzonitic granite. The porphyry stocks and dykes are NWW- or E-trending, outcrop along faults, and are several hundred meters long and a few or tens of meters wide. These stocks exhibit hydrothermal alteration, comprised of K-feldspar, plagioclase, and quartz with minor epidote and biotite, and are associated with porphyry-type Mo mineralization.

Four orebodies are mainly hosted in Neoproterozoic granitic gneisses, containing 88.3 Mt ores grading 0.058 % Mo, corresponding to a reserve of 51 Kt Mo in metal. The main orebody (M3) is about 960 m long and 480–800 m wide, with a lenticular or sheet-like shape. It dips northward or northwestward, with edges branching

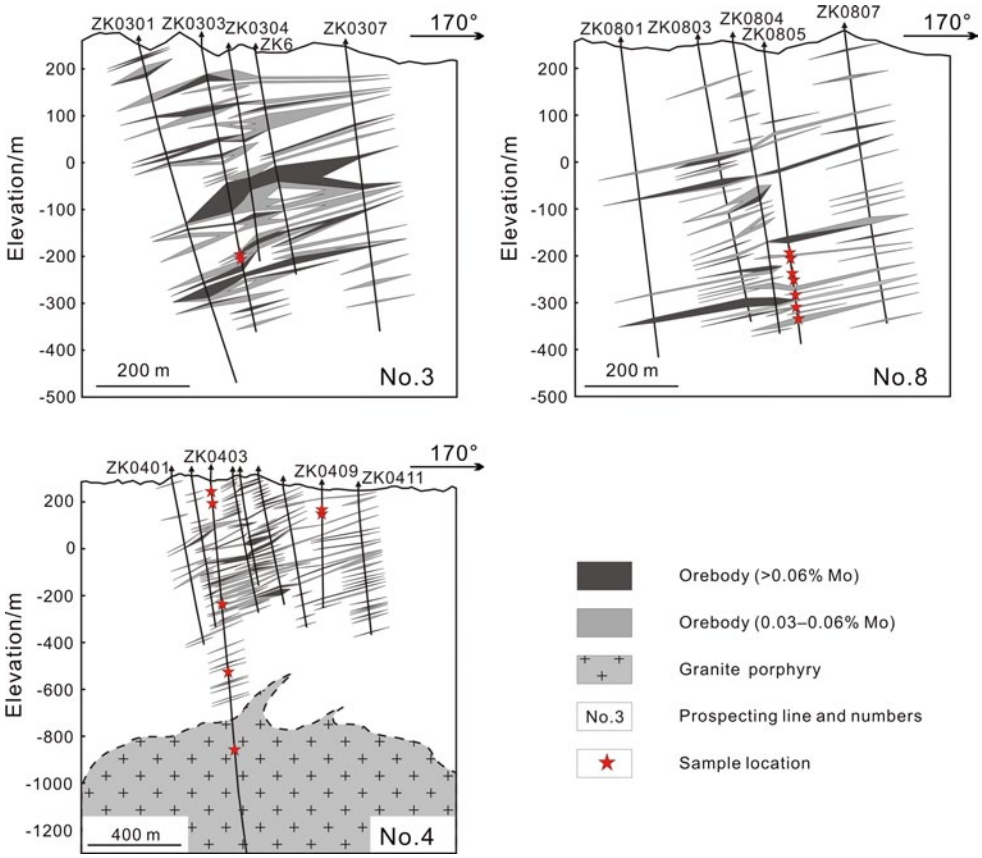

Fig. 3 Geological exploration profiles showing the shape of orebody

and pinching out (Fig. 3). The main ore minerals consist of molybdenite (Fig. 5b) and pyrite (Fig. 5a, c). Minor ore minerals include chalcopyrite (Fig. 5c), magnetite (Fig. 5a), and sphalerite (Fig. 5c). The main gangue minerals include quartz and K-feldspar, with lesser sericite, biotite, epidote, chlorite, and fluorite. Ore styles are disseminations, veinlets (Fig. 4b), stockworks, and breccias. The alteration assemblages at Yaochong deposit include the following: (1) potassic assemblage (Fig. 4c, f), which is characterized by feldspar and biotite as the predominant hydrothermal minerals and is present in the Yanshanian porphyry and wallrocks; (2) a quartz-dominated assemblage, which is widespread in the porphyry and wallrocks, in forms of quartz blocks and quartz ± sulfide stockworks; (3) a sericite-dominated assemblage, which is mainly represented by alteration of feldspar and biotite to sericite, with disseminated pyrite in veins and wallrocks; (4) propylitic assemblages (Fig. 5e), with chlorite, epidote, and calcite as predominant hydrothermal minerals; (5) carbonate-dominated assemblages (Fig. 5f), mainly characterized by carbonate veins; and (6) fluorite-bearing assemblages, mainly represented by disseminated purple fluorite grains.

According to vein crosscutting relationships, vein mineralogy and morphology, the hydrothermal mineralization and alteration processes are divided into four stages from early to late, as addressed below.

Stage 1 is marked by the barren quartz + K-feldspar veins in the porphyry and wall-rocks and are cut by the veins formed in later stages (Fig. 4a, b). Coeval alteration assemblages include potassic assemblages (Fig. 4a) and quartz-dominated assemblages, which are usually overprinted by fluorite and sericite-dominated assemblages. The veins are generally 0.2–4 cm thick and are composed of quartz and K-feldspar (Fig. 4a), with minor pyrite and/or magnetite (Figs. 4b, 5a). Pyrite mostly occurs as idiomorphic to hypidiomorphic cubes, sometimes coexisting with magnetite (Fig. 5a), is usually coarse-grained, with sizes of 0.5–3 cm, and generally borders the vein walls or grows as free-standing crystals.

Stage 2 veins are mainly 0.5–4 cm thick and mainly include two mineral assemblages of quartz + K-feldspar + molybdenite (Fig. 4c, e) and quartz + K-feldspar + molybdenite + pyrite (Fig. 4a, d). These assemblages also contain minor other sulfides, as well as sericite, biotite, fluorite, chlorite, and epidote. Molybdenite has a flaky habit (Fig. 5b) and occurs as fine-grained films coating cracks, or disseminated throughout the vein quartz and the contact zone (Fig. 4e), with uneven granularity ranging from 0.02 to 2 mm. Coeval alteration assemblages include

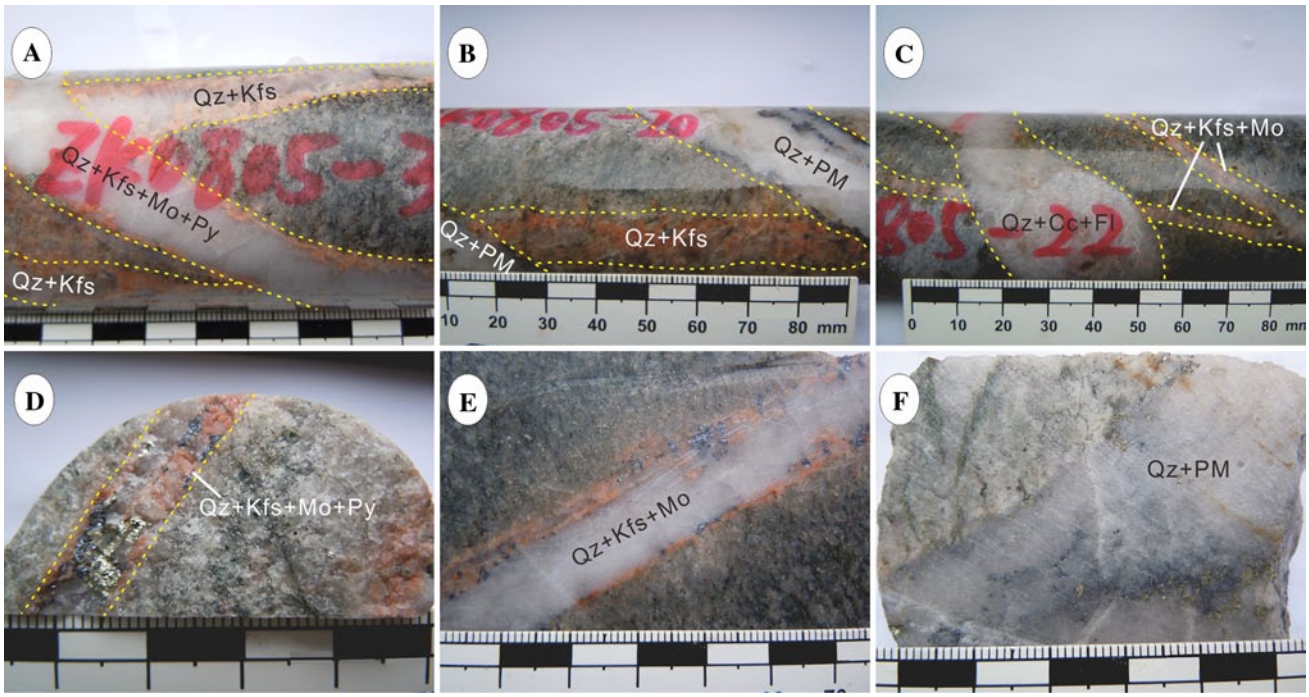

Fig. 4 Photographs showing aspects of the Yaochong Mo ores. **a** Stage 1 barren quartz-K-feldspar vein cut by stage 2 quartz-K-feldspar-molybdenite-pyrite vein; **b** stage 1 quartz-K-feldspar vein cut by quartz-polymetallic sulfides vein; **c** stage 2 quartz-K-feldspar-molybdenite vein cut by the stage 4 barren quartz-calcite-fluorite veins; **d** stage 2 quartz-K-feldspar-molybdenite-pyrite vein; **e** stage 2 quartz-K-feldspar-molybdenite vein; **f** stage 3 quartz-polymetallic sulfides vein. *Cc* calcite, *Kfs* K-feldspar, *Mo* molybdenite, *PM* polymetallic sulfides, *Py* pyrite, *Qz* quartz, *Fl* Fluorite

quartz-dominated, potassic feldspar-dominated, and sericite-dominated assemblages (Fig. 5d).

Stage 3 veins are 0.1–2 cm thick, mainly composed of quartz and polymetallic sulfides (Fig. 4b, f), forming stockworks. Potassium feldspar can be occasionally observed in this stage. The sulfides, including pyrite, chalcopyrite, tetrahedrite, galena, sphalerite, and molybdenite, occur as xenomorphic to idiomorphic grains (Fig. 5c) and are more complex than the other three stages. Conspicuous alteration assemblages with the veins are mainly quartz-dominated, sericite-dominated, propylite (Fig. 5e) and fluorite-dominated.

Stage 4 is typical of barren quartz ± carbonate ± fluorite veins. The veins are 0.3–4 mm thick and include quartz only, quartz + calcite (Fig. 5f), and quartz + calcite + fluorite (Fig. 4c) veins, with little or no sulfide. These veins crosscut the earlier veins and altered porphyry blocks (Fig. 4c).

Analytical methods

42 samples used in this study were collected from drill cores of ZK0303, ZK0403, ZK0409 and ZK0805 (Fig. 3), as well as porphyry dykes outcropping at the deposit.

Fluid inclusion measurement

42 samples used for fluid inclusion study are listed in Table 1. Double polished thin sections (<0.30 mm thick) were used for petrographical fluid inclusion studies, microthermometry, and laser Raman spectroscopy. Microthermometric measurements were carried out on a Linkam THMSG600 Heating–Freezing stage in the Fluid Inclusion Laboratory of the Institute of Geology for Mineral Resources, Beijing. Stage calibration was carried out at −56.6, −10.7, 0.0 and +374.1 °C using synthetic fluid inclusions supplied by FLUID INC. The precision of temperature measurements is ±0.2 °C for <30 °C, ±1 °C for the interval of 30–300 °C, and ±2 °C for temperatures >300 °C, respectively. Heating rate was generally 1–5 °C/min during the initial stages of each heating run and then reduced to 0.2–0.5 °C/min when close to the phase transformation points. Melting temperatures of solid CO_2 ($T_{m,CO2}$), freezing point of aqueous inclusions ($T_{m,ice}$), final melting temperatures of clathrate ($T_{m,cla}$), homogenization temperatures of CO_2 phase ($T_{h,CO2}$), dissolution temperatures of daughter minerals ($T_{m,d}$), and total homogenization temperatures of FIs (T_h) were measured.

The compositions of individual FIs, including vapor, liquid, and daughter mineral phases, were detected using laser Raman spectroscopy in Key Laboratory of Orogen

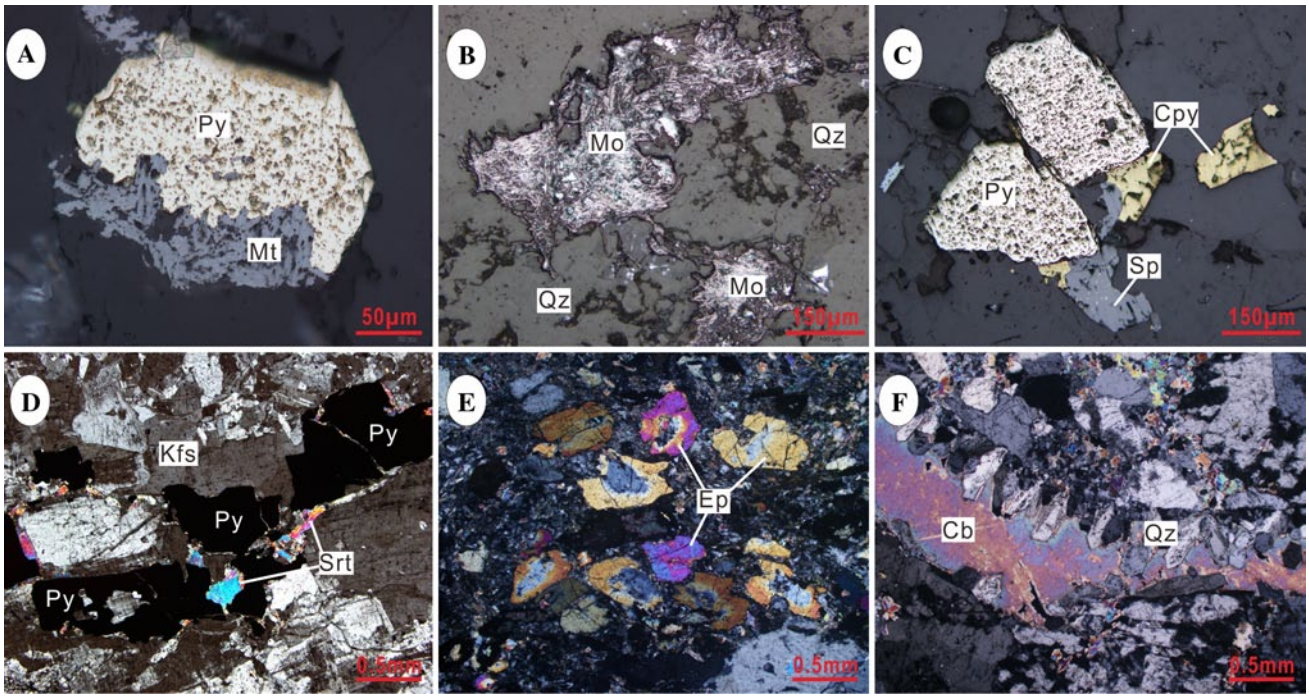

Fig. 5 Photomicrographs showing mineral assemblages of different stages. **a** Pyrite coexisting with magnetite in the stage 1 quartz-K-feldspar vein; **b** flaky molybdenite in the stage 2 quartz-K-feldspar-molybdenite vein; **c** pyrite, chalcopyrite and sphalerite with chalcopyrite minute inclusions, in the stage 3 quartz-polymetallic sulfides vein; **d** pyrite coexisting with sericite and K-feldspar in the stage 2 quartz-K-feldspar-molybdenite-pyrite vein; **e** epidotization; **f** the stage 4 barren quartz-carbonate vein, in which comb-shaped quartz developed. A, B and C are reflect light photos; **d**–**f** cross-polar photos. *Cb* carbonate, *Cpy* chalcopyrite, *Ep* epidote, *Kfs* K-feldspar, *Mo* molybdenite, *Mt* magnetite, *Py* pyrite, *Qz* quartz, *Sp* sphalerite, *Srt* sericite

and Crust Evolution, Peking University. The source was an argon laser with wave length of 514.5 nm and a source power of 1,000 mW. Integration time was 10 s, with 10 accumulations for each spectral line. The spectral resolution is ± 2 cm^{-1} with a beam size of 2 μm.

Salinities of CO_2-bearing and aqueous inclusions were calculated using the final melting temperatures of CO_2-clathrate (Collins 1979) and ice points (Bodnar 1993), respectively. Solid phases that did not dissolve at high temperatures were excluded from the salinity estimates.

Stable isotopic analysis

Nineteen representative samples from four different stages were selected for hydrogen and oxygen isotopic analysis. Oxygen was liberated from quartz separates (~20 mg) by reaction with BrF_5 (Clayton and Mayeda 1963) and converted to CO_2 on a platinum-coated carbon rod for $^{18}O/^{16}O$ measurements. Water of the fluid inclusions in quartz separates was released by heating the samples to above 500 °C by means of an inductive furnace and then reacted with zinc powder at 410 °C to generate hydrogen for δD (Friedman 1953). Carbon isotopic composition of fluid inclusion was measured on CO_2 of fluid inclusions in quartz. The CO_2 was released by thermal decrepitation and then collected, condensed, and separated in a liquid nitrogen–alcohol cooling trap (−70 °C) prior to measurement for $\delta^{13}C$.

Hydrogen, oxygen, and carbon isotopic analyses were performed with the Finnigan MAT253 mass spectrometer in the Stable Isotope Laboratory of the Institute of Mineral Resources, Chinese Academy of Geological Sciences, Beijing. The $\delta^{18}O$ and δD were reported in per mil relative to Vienna SMOW, with analytical uncertainty (1σ) of ±2 ‰ for δD and ±0.2 ‰ for $\delta^{18}O$. The $\delta^{13}C$ values were reported in per mil relative to PDB, and the analytical uncertainty (1σ) is less than ±0.2 ‰.

Fluid inclusion geochemistry

Fluid inclusion types

Four compositional types of fluid inclusion in veins are identified based on their phase associations at room temperature, phase transitions upon heating and cooling, and laser Raman spectroscopy. They are pure CO_2, mixed low-salinity CO_2, low-salinity aqueous, and solid-bearing, low-salinity aqueous inclusions (Fig. 6).

Table 1 Distribution of fluid inclusion in samples from the Yaochong Mo deposit

Stage	Sample no.	Drill hole	Depth (m)	Vein mineralogy	PC (%)	C (%)	W (%)	S (%)
I	YC-16a	ZK0303	444	Qz, Kfs		95		5
	YC-19	ZK0303	450	Qz, Kfs, Pl, Mt, Py		95		5
	0805-24	ZK0805	524	Qz, Kfs, Py	20	50	30	
	0805-29	ZK0805	489	Qz, Kfs, Mt, Py	5	95		
	0805-31a	ZK0805	478	Qz, Kfs	50	50		
	0805-34	ZK0805	480	Qz, Kfs, Py	40	60		
II	YC-12		0	Qz, Kfs, Pl, Py, Mo, Srt		45		55
	YC-16b	ZK0303	444	Qz, Kfs, Mo		100		
	YC-18	ZK0303	448	Qz, Kfs, Mo		95	5	
	YC-23a	ZK0409	101	Qz, Kfs, Py, Mo, Bi, Chl		85	15	
	0805-21b	ZK0805	550	Qz, Kfs, Py, Mo, Bi, Fl	5	95		
	0805-22a	ZK0805	556	Qz, Kfs, Mo, Py		100		
	0805-23a	ZK0805	575	Qz, Kfs, Mo, Py, Srt	15	75	10	
	0805-25	ZK0805	496	Qz, Kfs, Mo, Py, Srt, Fl	15	60		25
	0805-26b	ZK0805	492	Qz, Kfs, Py, Mo, Srt		80	20	
	0805-27	ZK0805	490	Qz, Kfs, Mo, Py, Srt		100		
	0805-28	ZK0805	488	Qz, Kfs, Mo, Py, Bi		85	15	
	0805-30	ZK0805	488	Qz, Kfs, Py, Mo, Mt, Fl, Srt	5	60	10	25
	0805-31b	ZK0805	478	Qz, Kfs, Mo, Bi	35	65		
	0805-32	ZK0805	479	Qz, Kfs, Py, Mo, Bi, Srt		100		
	0805-35	ZK0805	446	Qz, Kfs, Py, Mo, Srt, Bi, Chl, Ep		100		
	0805-36	ZK0805	434	Qz, Kfs, Py, Mo, Fl, Bi, Srt	5	70	10	15
	0805-37	ZK0805	460	Qz, Kfs, Py, Mo, Fl, Bi, Srt	10	90		
	0403-43	ZK0403	535	Qz, Kfs, Py, Mo, Bi, Srt	5	90	5	
	0403-44	ZK0403	54	Qz, Kfs, Py, Mo, Bi, Srt, Chl		95	5	
	0403-45	ZK0403	58	Qz, Kfs, Py, Mo, Bi, Srt, Chl		100		
	0403-47a	ZK0403	1,156	Qz, Kfs, Mo, Py, Srt		100		
III	YC-05		0	Qz, Kfs, Pl, Mo, Py, Cpy, Sp, Bi, Srt, Chl	5	55	40	
	YC-13		0	Qz, Pl, Mo, Py, Hem, Srt, Ep		5	85	10
	YC-14		0	Qz, Kfs, Mo, Py, Cpy		50	30	20
	YC-20	ZK0303	453	Qz, Kfs, Mo, Py, Cpy, Sp, Chl, Fl, Bi		100		
	YC-21	ZK0409	91	Qz, Mo, Fl		80	10	10
	YC-23b	ZK0409	101	Qz, Kfs, Mo, Py, Cpy, Sp, Bi, Chl		80		20
	YC-24	ZK0409	88	Qz, Kfs, Mo, Py, Cpy, Sp		90		10
	YC-25	ZK0409	87	Qz, Kfs, Py, Cpy, Sp		90		10
	0805-21a	ZK0805	550	Qz, Kfs, Mo, Py, Cpy	5	95		
	0805-26a	ZK0403	492	Qz, Fl, Mo		80	20	
	0403-42	ZK0403	824	Qz, Kfs, Pl, Cpy, Mo, Py, Sp, Bi, Srt, Chl		65	25	10
	0403-47b	ZK0403	1,156	Qz, Kfs, Py, Mo, Sp, Fl, Srt		70	5	25
IV	0403-41	ZK0403	105	Qz			100	
	0805-22b	ZK0805	556	Qz, Cc, Fl			100	
	0805-23b	ZK0805	575	Qz, Cc, Fl			100	

Bi biotite, *Cc* calcite, *Chl* chlorite, *Cpy* chalcopyrite, *Ep* epidote, *Fl* fluorite, *Hem* hematite, *Kfs* K-feldspar, *Mt* magnetite, *Mo* molybdenite, *Py* pyrite, *Qz* quartz, *Sph* sphalerite, *Srt* sericite

PC-type (pure CO_2 inclusions)

They are CO_2-only inclusions, containing liquid CO_2 or liquid CO_2 + vapor CO_2 at room temperature (Fig. 6a), and can be observed in quartz of stages 1, 2, and 3 veins. These inclusions have ellipsoidal or negative crystal shapes, with sizes of 5–15 μm. They usually occur in clusters or coexist with C-type inclusions.

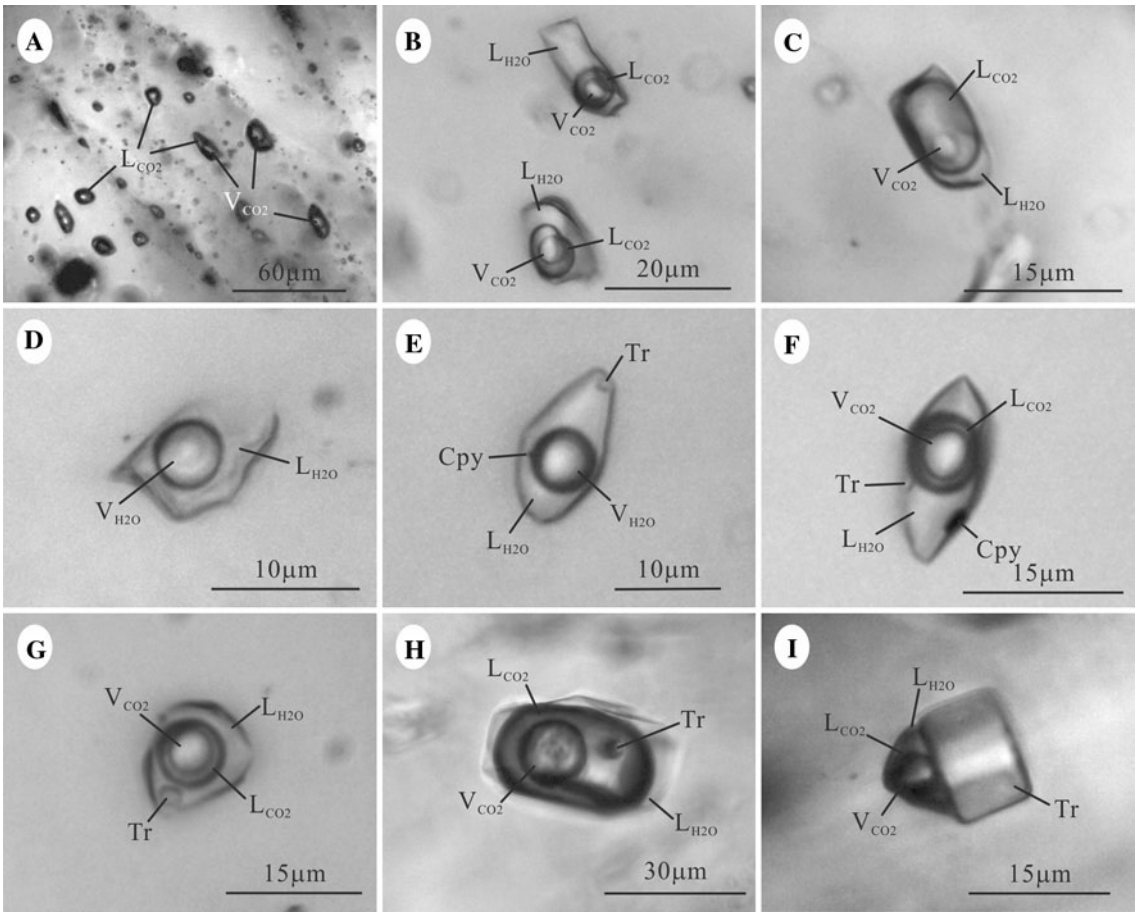

Fig. 6 Photomicrographs of fluid inclusions in the Yaochong Mo deposit. **a** The pure CO_2 inclusion group; **b** CO_2–H_2O inclusions rich in H_2O; **c** CO_2–H_2O inclusion rich in CO_2; **d** two-phase aqueous inclusion; **e** daughter chalcopyrite- and unidentified transparent mineral-bearing aqueous inclusion; **f** daughter chalcopyrite- and unidentified transparent mineral-bearing CO_2–H_2O inclusion; **g** CO_2–H_2O fluid inclusion containing an unidentified transparent crystal; **h** CO_2–H_2O fluid inclusion containing an unidentified transparent crystal in fluorite; **i** CO_2–H_2O fluid inclusion containing an unidentified transparent crystal in fluorite. V_{CO2} CO_2 vapor, L_{CO2} CO_2 liquid, V_{H2O} H_2O vapor, L_{H2O} H_2O liquid, *Cpy* chalcopyrite, *Tr* unidentified transparent solid mineral

C-type (CO_2-bearing inclusions)

The C-type FIs are the most abundant type in hydrothermal minerals, occupying nearly 75 % by volume of the total FIs. They are composed of two (liquid H_2O + CO_2-rich supercritical fluid) or three phases (liquid H_2O + liquid CO_2 + vapor CO_2) (Fig. 6b, c) at room temperature, with CO_2 phase accounting for 5–95 % of total volume. These inclusions have negative crystal, ellipsoid or irregular shapes and are generally 5–30 μm in diameter. They mainly grow in clusters or scatter throughout the sample.

W-type (aqueous inclusions)

The W-type inclusions are present in four types of veins, with about 15 % of the total inclusion populations. They consist of two phases (liquid H_2O + vapor H_2O) at room temperature (Fig. 6d), with vapor occupying 5–55 % of total volume. They have ellipsoid shape, with diameters of 5–15 μm. In stage 1 veins, few W-type inclusions can be identified as primary, with most occurring in well-defined secondary trials crosscutting the quartz crystals. The W-type inclusions in quartz and fluorite of stages 2 and 3 mainly occur in clusters or scatters, with the bubbles being identified by laser Raman spectroscopy to contain a minor amount of CO_2, although CO_2 was not observed during heating or cooling runs.

S-type (solid-bearing)

They consist of one or more solid phases or minerals and fluids with one to three phases (Fig. 6e–i) and show negative or ellipsoid shapes with the longest dimensions ranging from 10 to 40 μm. The S-type FIs can be divided into the SC-subtype with vapor CO_2 (Fig. 6f–i) and the SW-subtype with vapor H_2O (Fig. 6e). Chalcopyrite is the major opaque

Table 2 Microthermometric data of fluid inclusions in hydrothermal minerals from the Yaochong Mo deposit

Stage	Host	Type	N	$T_{m,CO2}$ (°C)	$T_{m,ice}$ (°C)	$T_{m,cla}$ (°C)	$T_{h,CO2}$ (°C)	T_h (°C)	*Salinity* (wt% NaCl)	*Density* (g/cm^3)
I	Quartz	*PC*	40	−57.3 to −56.6			6.5–31.1			0.52–0.88
		C	162	−58.3 to −56.6		2.1–8.4	17.5–31.1	288–501	3.19–13.12	0.45–0.89
		SC	6	−57.1 to −56.6		4.4–7.9	30.9–31.1	263–406	4.10–9.99	
		W	10		−2.8 to −1.5			262–329	2.60–4.60	
II	Quartz	*PC*	27	−58.0 to −56.6			3.3–31.1			0.52–0.91
		C	569	−58.4 to −56.6		3.7–8.7	21.5–31.1	225–380	2.62–11.01	0.51–0.95
		W	26		−7.0 to −0.7			202–307	1.22–10.49	
		SC	8	−58.0 to −56.6		3.7–8.0	26.4–31.1	303–354	3.95–11.01	
	Fluorite	*PC*	1	−56.6						
		C	48	−57.2 to −56.6		6.6–9.0	19.7–31.1	285–343	2.03–6.46	
		W	14		−4.0 to −2.0			226–255	3.39–6.45	
		SC	39	−57.2 to −56.6		6.6–8.8	26.8–31.1	243–359	2.42–6.46	
III	Quartz	*PC*	5	−57.2 to −56.6			20.9–30.9			0.53–0.76
		C	302	−59.4 to −56.6		4.4–8.8	22.1–31.1	172–345	2.42–9.99	0.69–0.99
		W	56		−6.4 to −1.1			168–314	1.91–9.73	
		SC	24	−59.5 to −56.6		4.4–7.9	26.7–31.1	198–309	4.14–9.99	
		SW	6		−5.6 to −3.5			185–293	5.71–8.68	
	Fluorite	*C*	8	−57.7		7.5–8.4	23.7–30.8	225–263	3.19–4.87	
		SC	9	−57.7		7.3–8.7	24.7–30.8	227–263	2.62–5.23	
IV	Quartz	*W*	71		−4.3 to −0.4			128–229	0.70–6.88	
	Fluorite	*W*	17		−4.5 to −0.2			130–286	0.35–7.17	

C C-type FIs, *W* W-type FIs, *S* S-type FIs, *SC* SC-subtype FIs, *SW* SW-subtype FIs, $T_{m,CO2}$ melting temperature of solid CO_2, $T_{m,cla}$ melting temperature of clathrate, $T_{m,ice}$ last ice-melting temperature; $T_{h,CO2}$ homogenization temperature of the CO_2 phase; T_h, total homogenization temperature; *N* number of fluid inclusions analyzed; and the Th with * stands for the homogenization temperature of all the fluid phases in the S-type FIs

mineral (Fig. 6e, f), whereas transparent minerals include calcite and some unknown minerals that are insensitive to laser Raman spectroscopy (Fig. 6e–i). At the Yaochong deposit, it is noted that no halite-bearing inclusions have been observed, suggesting that the fluids are likely NaCl-poor, relative to the porphyry mineral systems in the Circum–Pacific rim which commonly contain halite-bearing fluid inclusions (Lu et al. 2004; Yang et al. 2013b). The S-type FIs are present in the veins formed in stages 1–3.

Microthermometry

Microthermometric measurements were carried out on more than 1,400 fluid inclusions. The results are summarized in Table 2 and Figs. 6 and 7, which show a decreasing trend in temperatures, salinities and CO_2 contents from stage 1 to stage 4.

Stage 1

Fluid inclusions in stage 1 quartz are generally dominated by C-type (followed by PC-type, with minor of S- and W-types). The PC-type FIs yield melting temperatures ($T_{m,CO2}$) of −57.3 to −56.6 °C, equal to or close to the triple-phase point (−56.6 °C) of CO_2, suggesting the absence or negligible amounts of other gas species. This was confirmed by laser Raman analysis. The homogenization temperatures of CO_2 ($T_{h,CO2}$) to liquid or to vapor range from 6.5 to 31.1 °C.

The C-type FIs, with carbonic phase accounting for 20–95 vol%, yield $T_{m,CO2}$ of −58.3 to −56.6 °C, suggesting that the carbonic phase contains a trace amount of other gases than CO_2. The clathrate melting temperatures ($T_{m,cla}$) range from 2.1 to 8.4 °C, corresponding to salinities of 3.2–13.1 wt% NaCl eq. The CO_2 phases homogenized at temperatures of 17.5–31.1 °C in three modes, i.e., to liquid, to vapor, and by critical behavior. Some of the C-type FIs with >50 vol% CO_2 are decrepitated at temperatures of 200–357 °C before total homogenization, and the rest totally homogenized to liquid, to vapor, or by the critical behavior at temperatures of 288–501 °C(T_h), clustering at 320–400 °C. These measurements correspond to densities of 0.45–0.89 g/cm^3.

The S-type FIs are dominated by SC-subtype, with carbonic phases accounting for 25–70 %. The daughter

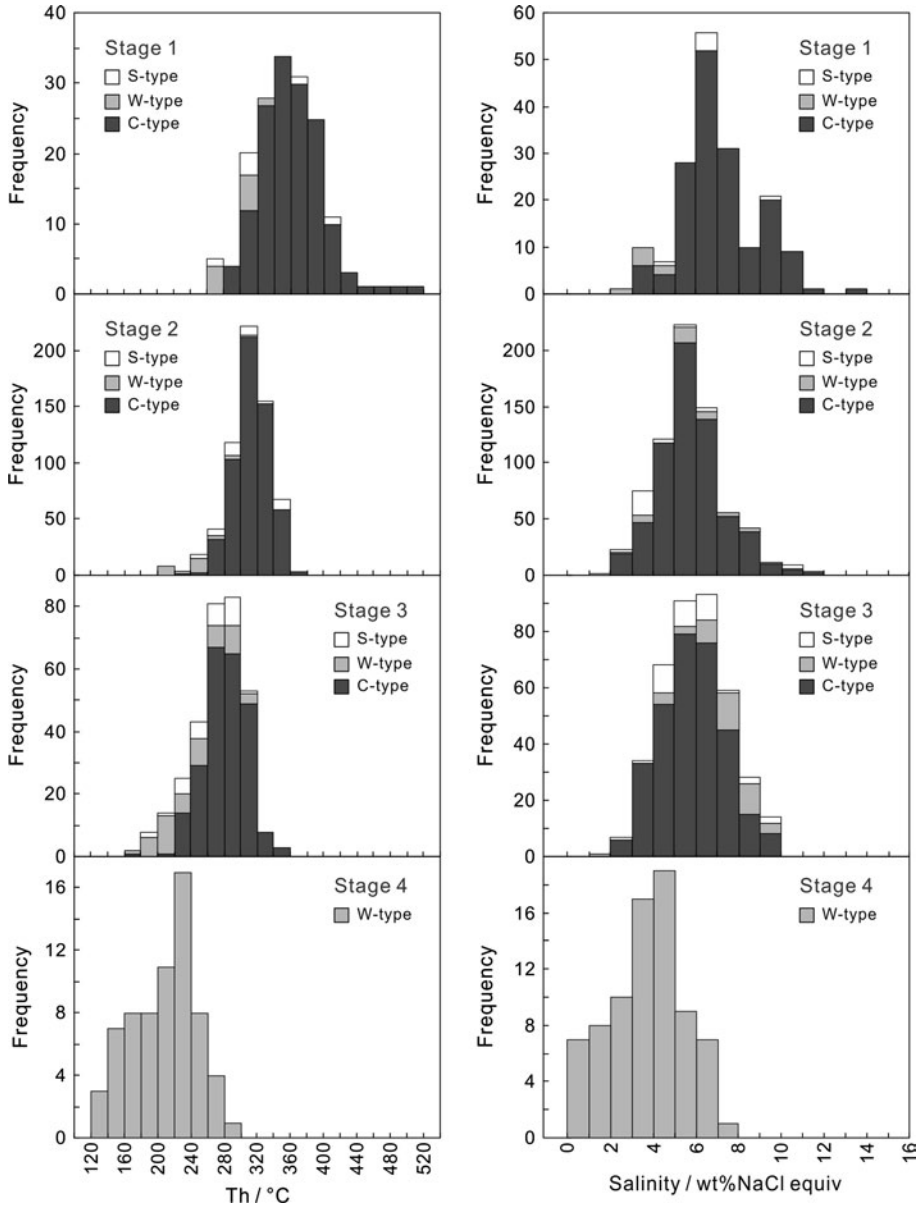

Fig. 7 Histograms of homogenization temperatures and salinities of fluid inclusions in different stage minerals at Yaochong Mo deposit

minerals did not melt during heating runs. They yielded $T_{m,CO2}$ values of −57.1 to −56.6 °C, $T_{m,cla}$ values of 4.4–7.9 °C, salinities of 4.1–10.0 wt% NaCl eq., excluding the contribution of daughter minerals. The carbonic phase homogenized to liquid or by critical behavior at temperatures of 30.9–31.1 °C. The fluid phases totally homogenized to vapor, to liquid, or by the critical behavior at temperatures of 263–406 °C.

The W-type FIs, with vapor bubbles accounting for 20–25 vol%, yield ice-melting temperatures of −2.8 to −1.5 °C, and salinities of 2.6–4.6 wt% NaCl eq. They are mainly homogenized to liquid at temperatures of 262–329 °C, indicating that some secondary FIs are incorporated.

Stage 2

Fluid inclusions in stage 2 quartz and fluorite consist of 10 % PC-type, 75 % C-type, 5 % W-type, and 10 % S-type inclusions. The PC-type FIs yield melting temperatures of −58.0 to −56.6 °C and homogenization temperatures of 3.3–31.1 °C. The carbonic phases in C-type FIs account for 10–95 vol% and yield $T_{m,CO2}$ of −58.4 to −56.6 °C, showing a small amount of other gases. The clathrate mainly dissociates at temperatures ($T_{m,cla}$) of 3.7–9.0 °C, yielding salinities of 2.0–11.0 wt% NaCl eq. The FIs partially homogenized to liquid, to vapor, or by the critical behavior at 19.7–31.1 °C and totally homogenized mainly to liquid or by critical behavior

and, in a small number of cases, to vapor, at temperatures of 225–380 °C (mainly 280–360 °C). Some of the FIs decrepitated at temperatures of 240–379 °C before homogenization. The fluid densities were calculated at between 0.51 and 0.95 g/cm^3. As identified by Raman spectroscopy, daughter minerals in the S-type FIs include chalcopyrite, calcite, and unidentified transparent crystals. The daughter minerals did not melt in the heating runs. The fluid phases homogenized to liquid or by critical behavior at temperatures of 243–359 °C. The vapor phase was mainly CO_2, accounting for 10–95 vol%. The SC-subtype FIs yield $T_{m,CO2}$ of −58.0 to −56.6 °C, $T_{m,cla}$ of 3.7–8.8 °C, and salinities of 2.4–11.0 wt% NaCl eq. The carbonic phases homogenized divergently to liquid, to vapor, or by critical behavior, at the temperatures of 26.4–31.1 °C.

The W-type FIs, with vapor bubbles occupying 5–35 vol%, yielded ice-melting temperatures of −7.0 to −0.7 °C, and salinities of 1.2–10.5 wt% NaCl eq. They mainly homogenized to liquid at temperatures between 202 and 307 °C, indicating that some secondary FIs were incorporated.

Stage 3

The stage 3 minerals contain FIs of approximately 74 % C-type, 15 % W-type, 10 % S-type, and 1 % PC-type. The PC-type FIs yielded $T_{m,CO2}$ of −57.2 to −56.6 °C and homogenization temperatures of 20.9–30.9 °C. The C-type FIs yielded $T_{m,CO2}$ of −59.4 to −56.6 °C, $T_{m,cla}$ of 4.4–8.8 °C, $T_{h,CO2}$ of 22.1–31.1 °C, and T_h of 172–345 °C (clustering at 240–320 °C), and corresponding to salinities of 2.4–10.0 wt% NaCl eq. and densities of 0.69–0.99 g/cm^3. The FIs mostly homogenized to liquid, but some of them decrepitated at temperatures of 198–342 °C in the heating runs before total homogenization.

The S-type FIs usually contain chalcopyrite and unknown transparent minerals as daughter crystals which did not melt during heating process. Their fluid phases homogenized to liquid at temperatures of 185–309 °C. Aqueous phases in SW-subtype FIs show ice-melting temperatures of −5.6 to −3.5 °C, corresponding to salinities of 5.7–8.7 wt% NaCl eq. The carbonic phases of SC-subtype occupy 10–50 vol%, while aqueous vapor of SW-subtype accounts for 10–20 vol%. The SC-subtype FIs yield $T_{m,CO2}$ of −59.5 to −56.6 °C, $T_{m,cla}$ of 4.4–8.7 °C, and salinities from 2.6 to 10.0 wt% NaCl eq. The carbonic phases homogenized divergently to liquid, to vapor, or by critical behavior, at the temperatures of 24.7–31.1 °C.

The W-type FIs yielded ice-melting temperatures of −6.4 to −1.1 °C, homogenization temperatures of 168–314 °C, corresponding to salinities of 1.9–9.7 wt% NaCl eq (Fig. 8).

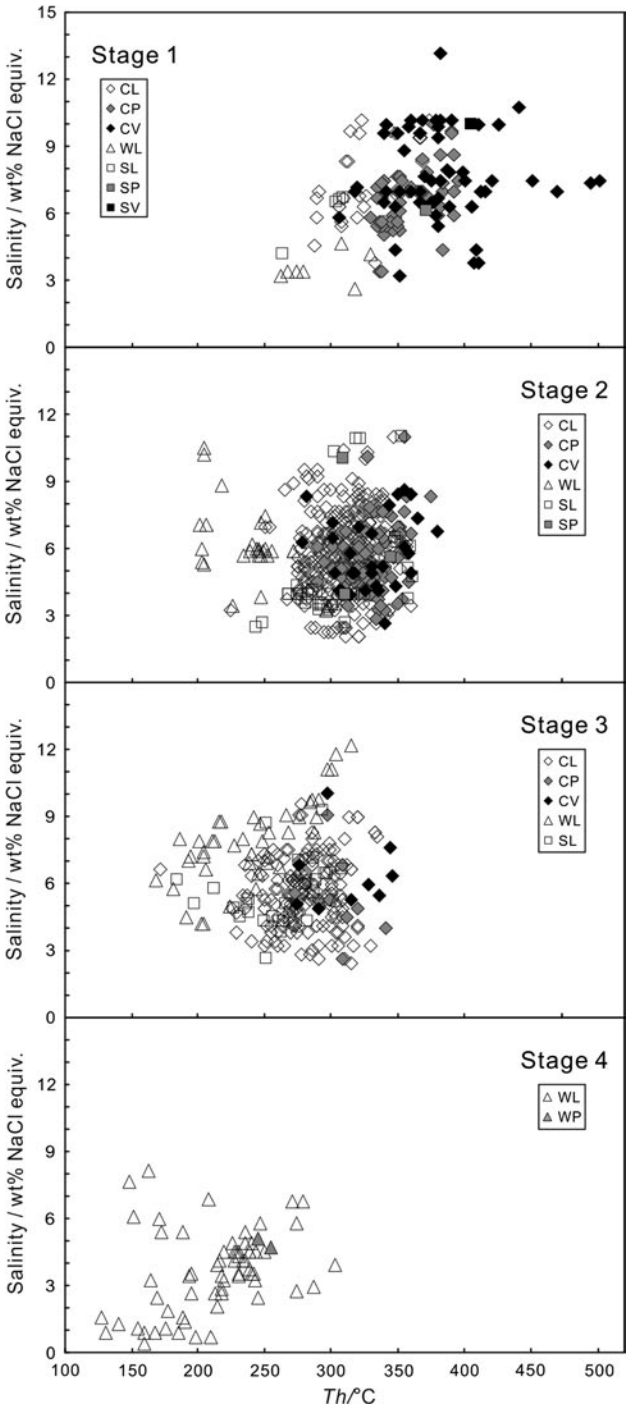

Fig. 8 Homogenization temperature (to liquid, vapor or by critical behavior) versus salinity of individual fluid inclusions

Stage 4

Fluid inclusions in stage 4 minerals are very simple, with the W-type only observed. All the FIs homogenized to liquid at temperatures of 128–286 °C and yielded freezing points of −4.5 to −0.2 °C, with corresponding salinities of 0.4–7.2 wt% NaCl eq.

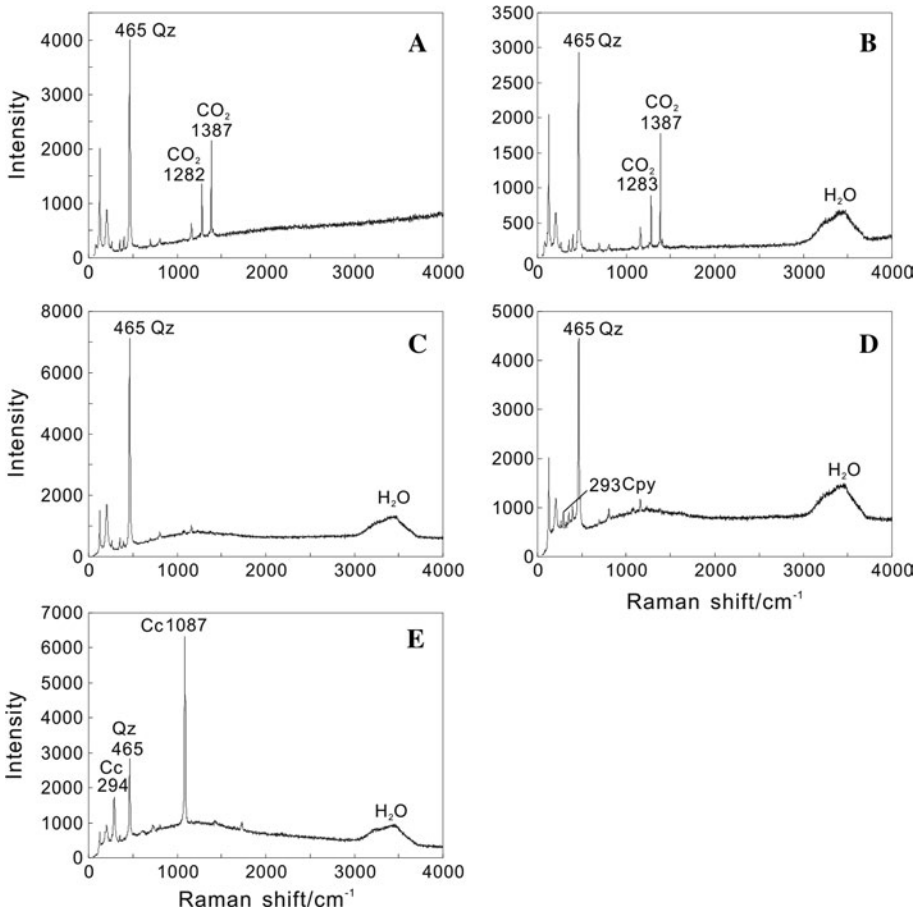

Fig. 9 The LRM spectra of fluid inclusions. **a** CO_2-spectrum of the PC-type fluid inclusion; **b** H_2O- and CO_2-spectra of the C-type fluid inclusion; **c** H_2O-spectrum of the W-type fluid inclusion; **d** daughter chalcopyrite in the S-type fluid inclusion; **e** daughter calcite in the S-type fluid inclusion

Laser Raman spectroscopy

Laser Raman spectroscopy shows that the similar type FIs from different stages mainly have similar fluid compositions. The spectra of PC-type FIs only showed major peaks of CO_2 (1,282 and 1,387 cm^{-1}) (Fig. 9a), suggesting that the CO_2 is the dominant component. The vapor phases of C-type FIs were dominated by CO_2, while the liquid phases were composed of H_2O and CO_2 (Fig. 9b), respectively. The vapor and liquid phases of the W-type FIs dominated by H_2O (Fig. 9c), but some W-type FIs contained small quantities of CO_2 in the vapor bubbles. The vapor phase of SC-subtype FIs was dominated by CO_2 and the liquid contained CO_2 and H_2O, while the vapor and liquid phases of SW-subtype were composed of H_2O. The spectra of opaque daughter minerals had the peak of chalcopyrite (293 cm^{-1}) (Fig. 9d). Some transparent daughter minerals had two peaks of 294 and 1,087 cm^{-1} (Fig. 9e) that are characteristics of calcite.

Pressure–temperature–depth estimates

According to Diamond (1994), if inclusions formed in the immiscible two-phase fluid, the trapping pressure can be approximated from end-member inclusions trapped nearest the solvus. At Yaochong, fluid immiscibility is evidenced based on the criteria outlined by Roedder (1984). In stage 1, 2, and 3, PC-type and C-type inclusions were trapped as primary clusters and thus interpreted as contemporaneous trapping. Accordingly, these inclusions have been selected to estimate trapping pressures. Based on the minimum and maximum densities, the range of isochores of PC-type and C-type FIs is defined on the P–T diagram using the Flincor program (Brown 1989) and the formula of Bowers and Helgeson (1983) for the CO_2 and the H_2O–CO_2–NaCl system. Taking the T_h averages of 363 ± 36, 314 ± 21, and 275 ± 24 °C for the FIs within the quartz of stages 1–3 into calculation, the minimum trapping pressures were estimated to be 69–248, 62–201, and 81–131 MPa, respectively (Fig. 10).

Considering the characteristics of porphyry-type mineralization, i.e., pulsating hydraulic broken-and-healing caused by fluid boiling and precipitation, the fluid system can be interpreted as a state of frequent alternations between supralithostatic to lithostatic and hydrostatic pressures. Therefore, the lowest trapping pressure of FIs represents the hydrostatic system, whereas the highest trapping pressure reflects the lithostatic to supralithostatic system.

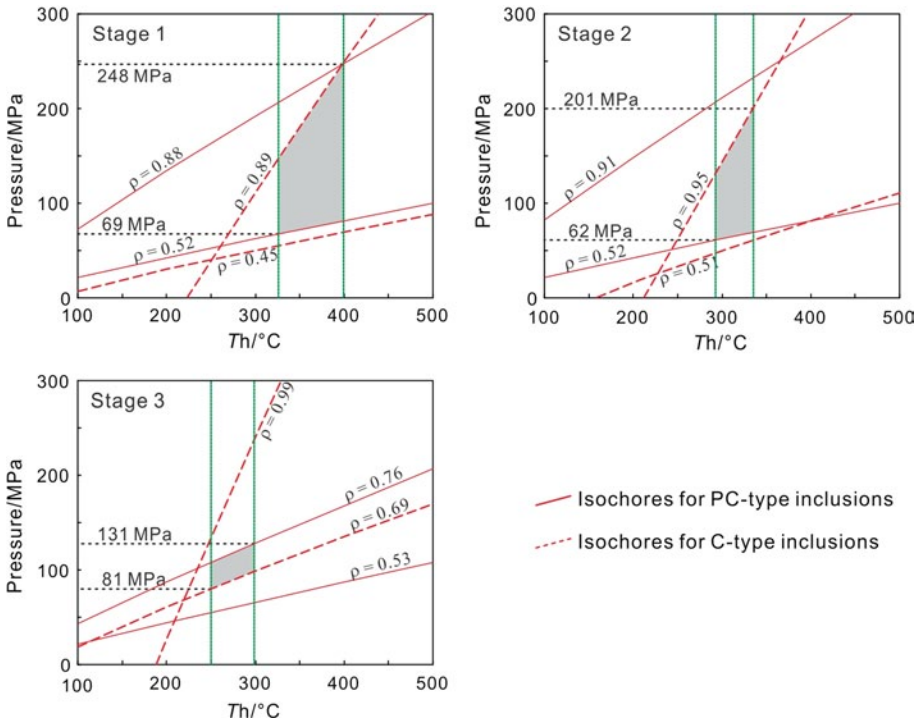

Fig. 10 The trapping pressure estimation diagrams for Yaochong deposit. Isochores of the PC-type and C-type fluid inclusions of stage 1, 2, and 3 veins, with the minimum and maximum densities and average homogenization temperatures with 1σ standard deviation, respectively

According to the estimated trapping pressure of the Yaochong deposit, the stage 1 barren veins were likely formed at depth of 6.9–8.9 km, while the mineralization of stages 2 and 3 likely occurred at depth of 6.2–7.2 and ~4.7 km, respectively, given that the average density of gneisses (the main host-rocks at Yaochong deposit) is 2.8 g/cm^3. Hence, we can draw a conclusion that the initial Mo mineralization at Yaochong deposit took place at a depth no shallower than 5.0 km.

H–O–C isotope geochemistry

Table 3 lists the analytical results of $\delta^{18}O_Q$, δD, and $\delta^{13}C_{CO2}$. The $\delta^{18}O_{H2O}$ values of ore-forming fluids are calculated with the equation of $1000 \ln \alpha_{quartz-H2O} = 3.38 \times 10^6 T^{-2}$–3.40 (Clayton et al. 1972) using homogenization temperatures of fluid inclusions for calculation. The calculated $\delta^{18}O_{H2O}$ of stage 1 veins are between 3.8 and 6.9 ‰ (Table 3), with an average of 5.0 ‰; the δD_{H2O} values are between −74 and −67 ‰, averaging at −71 ‰. These values mostly plot adjacent to the magmatic water box (Fig. 11). The $\delta^{18}O_{H2O}$ of stage 2 and stage 3 veins ranges from 2.5 to 3.3 ‰ and 0.9 to 2.4 ‰, averaging at 2.9 and 1.7 ‰, respectively; the δD_{H2O} values range from −80 to −55 ‰ and −72 to −58 ‰, respectively. These samples are plotted between the magmatic water box and the meteoric water line, suggesting that the fluids were mixtures of magmatic and meteoric water (Fig. 11). The $\delta^{18}O_{H2O}$ of stage 4 veins ranges from −1.3 to 0.6 ‰, with δD_{H2O} ratios ranging from −68 to −65 ‰, being typical of meteoric water. From stage 1 to stage 4, the data points generally shift from adjacent to the magmatic water box toward the meteoric water line from early to late (Fig. 1). Despite this, it should be pointed out that the inflow of meteoric water reduced the $\delta^{18}O$ values of the fluids, but did not to lower the δD_{H2O} values, as the δD values of the Mesozoic meteoric water were between −70 and −60 ‰ in the area (Zhang 1989).

Two samples of the stage 1 veins yield $\delta^{13}C_{CO2}$ values of −2.3 and −1.3 ‰ and are significantly higher than those of organic matter (−27 ‰), atmospheric CO_2 (−8 ‰, Schidlowski 1998), dissolved CO_2 in fresh water (−9 to −20 ‰, Hoefs 1997), continental crust (−7 ‰, Faure 1986), and mantle (−5 to −7 ‰, Hoefs 1997), but similar to or slightly higher than the igneous rocks (−3 to −30 ‰). This suggests that the CO_2 of initial fluids was probably sourced from a magmatic system or from a magmatic system contaminated by a carbonate-bearing context. The $\delta^{13}C_{CO2}$ values of stage 2 and stage 3 mineralized veins range from 0.1 to 2.7 ‰ and from 0.1 to 1.1 ‰, with averages of 1.2 and 0.6 ‰, respectively. Compared to the early veins, the increase in $\delta^{13}C$ values suggests that the fluids uptake ^{13}C from the wall-rocks during fluid–rock interaction and that the wall-rocks may have positive $\delta^{13}C$ values (Tang et al. 2011, 2013). This interpretation is supported by the significantly positive $\delta^{13}C$ values (1.7–5.7 ‰, Fu et al. 1998; Zheng et al. 1998; Rumble et al. 2000) of the marbles coexisting with eclogites and granitic gneisses, which are the main lithologies of the wall-rocks of the Yaochong deposit.

Table 3 The H–O–C isotope compositions (‰) of the Yaochong Mo deposit

Stage	Sample no.	Depth (m)	Vein mineralogy	Th (°C)	$\delta^{18}O_Q$	$\delta^{18}O_{H2O}$	δD	δC_{CO2}
I	YC-19	450	Qz, Kfs, Pl, Mt, Py	390	11.2	6.9	−73	−2.3
	0805-29	489	Qz, Kfs, Mt, Py	380	9.6	5.1	−71	−1.3
	0805-31a	478	Qz, Kfs	400	8.2	4.1	−67	
	0805-34	480	Qz, Kfs, Py	390	8.1	3.8	−74	
II	0805-26b	492	Qz, Kfs, Py, Mo, Srt	360	8.3	3.3	−55	
	0805-28	488	Qz, Kfs, Mo, Py, Bi	350	8.1	2.8	−59	
	0805-30	488	Qz, Kfs, Py, Mo, Mt, Fl, Srt	350	7.9	2.6	−66	1.1
	0805-32	479	Qz, Kfs, Py, Mo, Bi, Srt	350	7.8	2.5	−61	
	0805-35	446	Qz, Kfs, Py, Mo, Srt, Bi, Chl, Ep	350	8.2	2.9	−80	0.7
	0805-36	434	Qz, Kfs, Py, Mo, Fl, Bi, Srt	360	8.3	3.3	−73	0.1
	0403-43	535	Qz, Kfs, Py, Mo, Bi, Srt	370	8.0	3.2	−78	2.7
III	YC-21	91	Qz, Mo, Fl	330	7.7	1.8	−63	1.1
	YC-25	87	Qz, Kfs, Py, Cpy, Sp	340	8.0	2.4	−72	0.1
	0805-21a	550	Qz, Kfs, Mo, Py, Cpy	290	8.2	0.9	−71	
	0805-26a	492	Qz, Fl, Mo	320	8.2	2.0	−58	
	0403-42	824	Qz, Kfs, Pl, Cpy, Mo, Py, Sp, Bi, Srt, Chl	300	8.2	1.3	−70	
	0403-47b	1,156	Qz, Kfs, Py, Mo, Sp, Fl, Srt	300	8.4	1.5	−66	
IV	0805-22b	556	Qz, Cc, Fl	245	7.9	−1.3	−65	
	0805-23b	575	Qz, Cc, Fl	280	8.2	0.6	−68	

Bi biotite, *Cc* calcite, *Chl* chlorite, *Cpy* chalcopyrite, *Ep* epidote, *Fl* fluorite, *Hem* hematite, *Kfs* K-feldspar, *Mt* magnetite, *Mo* molybdenite, *Py* pyrite, *Qz* quartz, *Sph* sphalerite, *Srt* sericite

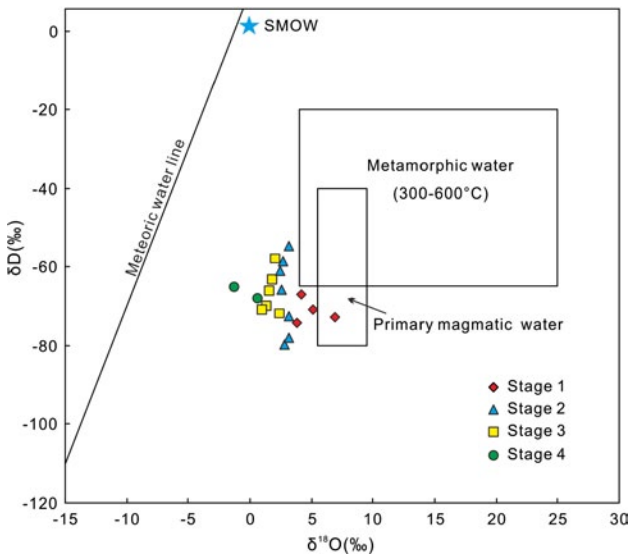

Fig. 11 The δD–$\delta^{18}O$ plot for the Yaochong Mo deposit (Base map after Taylor 1974)

Discussion

The CO_2-rich, NaCl-poor fluid system

Traditionally, the vapor-rich aqueous FIs with or without daughter minerals are considered as indicators of magmatic–hydrothermal systems (Cline and Bodnar 1991; Bodnar 1995; Ulrich and Heinrich 2001; Lickfold et al. 2003; Lu et al. 2004; Masterman et al. 2005; Klemm et al. 2007, 2008), but CO_2-bearing inclusions in magmatic–hydrothermal systems have only recently been reported, particularly in the continental collision settings, for instances, the Wunugetu Cu–Mo deposit, Inner Mongolia (Li et al. 2012b); the Yuchingling Mo deposit, Henan (Li et al. 2012c); the Tangjiaping Mo deposit, Henan (Yang et al. 2008; Chen and Wang 2011); the Baishan Mo deposit, Xinjiang (Xiang et al. 2013); the Trout Lake Mo deposit, British Columbia (Linnen and William-Jones 1990); Fort Knox Au deposit, Alaska (McCoy et al. 1997); Vasilkovskoe Au deposit, Kazakstan (Spiridinov 1996); and Kyzyltau W–Sn deposits (Graupner et al. 1999). The ore-forming fluid system at the Yaochong Mo deposit in Dabie Shan is compositionally carbonic-dominated, evidenced by numerous C-type FIs and the occurrence of PC-type and SC-subtype FIs.

To explain the contrasting CO_2 contents of magmatic–hydrothermal systems formed in continental collision settings and volcanic arcs (Nash 1976; Cline and Bodnar 1991; Bodnar 1995; Phillips and Zhou 1999; Lu et al. 2004), Chen et al. (2007b, 2008, 2009) and Chen and Li (2009) proposed that the ore-forming fluids of porphyry systems formed in volcanic arcs were mainly derived from metamorphic dehydration of subducted oceanic slab (Sillitoe 1972; Richards 2003),

which can be roughly regarded as "altered oceanic basalt" (NaCl-brine or seawater percolated oceanic crust), and thereby, rich in H_2O, NaCl, but poor in CO_2 (or carbonate), K, and F. Consequently, abundant aqueous inclusions and rare (if any) CO_2-bearing inclusions, with or without daughter minerals, characterize porphyry deposits formed in oceanic subduction-related island arcs. By contrast, porphyry-type mineral systems developed in syn- or/and post-collision settings must be sourced from the thickened continental crust that is poor in H_2O and NaCl, but rich in CO_2, K, and F relative to oceanic crust (Chen and Li 2009; Tang et al. 2008, 2009). As a result, the CO_2-rich ore-forming fluids, evidenced by CO_2-bearing FIs with or without daughter minerals, can be considered as a diagnostic marker of porphyry ore systems formed in intracontinental collision regimes during or after orogenesis.

The ore-forming fluids of the Yaochong deposit were also NaCl-poor as indicated by the absence of halite-bearing FIs in hydrothermal minerals. The S-type FIs identified at the Yaochong deposit usually contain chalcopyrite daughter minerals or other transparent minerals such as calcite, but no halite has been observed yet. This phenomenon was reported at the Qian'echong Mo deposit in Dabie Shan and was related to the low NaCl activity in the initial ore-forming fluids (Yang et al. 2013b). Here we propose that the relatively low NaCl activity results from high contents of Ca, K, and F in the fluids, which can be supported by the development of calcite as daughter mineral and the widespread K-feldspathization and fluoritization (see above). Certainly, the fluids, being poor in NaCl and rich in Ca, K, and F, are difficult to relate to oceanic crust, but easy to link with continental lithosphere.

Fluid evolution and Mo mineralization

Fluid inclusions, as the "fossil" of ancient fluid systems, particularly the primary FIs in the earliest stage, can reveal the nature and genesis of the original fluids (Ulrich et al. 1999; Chen et al. 2007b; Mernagh et al. 2007; Pirajno 2009, 2013; Fan et al. 2011). Based on petrographic relationships and microthermometric results of FIs presented above, we recover the fluid evolution history at Yaochong deposit.

The original fluids, recorded by numerous assemblages of CO_2-bearing inclusions with high homogenization temperature (up to 500 °C) and trapping pressure, were most likely magmatic in origin and carbonic, K-rich, and probably Mo- and Fe-rich in composition. Stage 1 mineralization and alteration mainly occurred at 320–400 °C and 69–248 MPa, characterized by barren quartz + K-feldspar veins and K-feldspathization and silicification. Due to high CO_2 activity and high oxygen fugacity, the sulfur activity was constrained, and little sulfides were formed.

K-feldspathization and formation of quartz + K-feldspar veins in stage 1 consumed alkali ions and reduced the *p*H values of the fluids. Increasing H^+ activity led to CO_2 escape from the fluids via $2H^+ + CO_3^{2-} \rightarrow H_2O + CO_2\uparrow$, and thereby, together with formation of magnetite, it resulted in fO_2 decrease and S^{2-} activity increase, facilitating deposition of sulfides, such as molybdenite and pyrite. Large-scale CO_2 separation and escape possibly caused phase separation followed by inflow of meteoric water. This is the stage 2 mineralizations mainly occurred at temperatures of 280–360 °C and pressures of 62–201 MPa.

In stage 3, increasing amounts of meteoric water flowed into and mixed with the magmatic fluids, which cooled the hydrothermal system and caused precipitation of polymetallic sulfides, together with phyllic alteration. The fluids gradually became CO_2-poor in composition and meteoric-dominated, as indicated by the H–O isotope signature. The mineralization and alteration mainly occurred at temperatures of 240–320 °C and pressures of 81–131 MPa.

After the formation of quartz + K-feldspar + molybdenite and quartz + polymetallic sulfide veins, temperatures and salinities of the fluid system decreased further, estimated about 140–260 °C and 0.4–7.2 wt% NaCl eq., respectively. The CO_2/H_2O ratios of the fluids also decreased dramatically, as indicated by the lack of C-, PC- and S-type inclusions and prevalence of W-type inclusions in the stage 4 veins. This type of vein contributed little to mineralization and represented the waning hydrothermal system.

Available data show that the porphyry systems in Dabie Shan, such as Qian'echong (Yang et al. 2013b), Dayinjian (Li et al. 2010) and Tangjiaping (Yang et al. 2008; Chen and Wang 2011) Mo deposits, share a similar fluid nature and evolution with the Yaochong deposit. Fluids forming these deposits were initially CO_2-rich and high salinity, as evidenced by the observations of PC-, C-, and S-type FIs in earlier hydrothermal stages and then evolved to low temperature, low salinity and CO_2-poor. The H–O–C isotope data indicate that the fluids evolved from magmatic to meteoric.

The estimated trapping pressures of C-type FIs decrease gradually, but significantly, from early to late. This accords with many porphyry systems, such as the Qian'echong Mo deposit in Dabie Shan (Yang et al. 2013b), the Yuchiling (Li et al. 2012c) and Shangfanggou (Yang et al. 2013a) Mo deposits and the Qiyugou gold deposit (Fan et al. 2011; Li et al. 2012a) in eastern Qinling Orogen, Baishan Mo deposit in East Tianshan (Xiang et al. 2013), and Chehugou Mo–Cu deposit in southern Great Hinggan Range (Meng et al. 2013), which were interpreted to have formed in a rapid crust uplifting setting caused by synorogenic crustal thickening or post-orogenic delamination of lithospheric root (Chen 2013; Pirajno 2013). Therefore, the Yaochong deposit might have formed in a rapid crust uplifting process caused by post-collisional lithospheric delamination in the

Table 4 Comparison between Yaochong and Climax-type porphyry Mo systems

	Characteristics	Yaochong	Climax-type
Intrusion	Type of intrusion	Stock	Stock
	Intrusive phases	Single intrusion of granite	Multiple intrusions of granites
Mineralization	Cogenetic rock type	Granite porphyry	Granite porphyry
	Style of mineralization	Stockwork veinlets, minor disseminations	Stockwork veinlets, minor disseminations
	Orebody shape	Lenticular or sheet-like	Inverted cup
	Average ore grade	0.058 %	0.30–0.45 %
	Ore-associated minerals	Pyrite, chalcopyrite, sphalerite, fluorite, sericite, K-feldspar	Pyrite, wolframite (huebnerite), cassiterite, stannite, bismuth sulfosalts, chalcopyrite (rare), fluorite, topaz, sericite
Alteration	Hydrothermal alteration	Intense potassic alteration, weak sericitization and propylitic alteration	Potassic alteration, sericitization, and propylitic alteration
Fluids	Inclusion type	Pure CO_2, CO_2-bearing, aqueous, lack of brine inclusions	Aqueous, brine, with or without CO_2-bearing
	Brine homogenization mode		By vapor disappearance or halite dissolution
	Original phase	CO_2-rich Vapor	Low-salinity liquid with moderate to low CO_2
	Temperature	130–500 °C	200–600 °C
	Tectonic setting	Post-collision, extensional	Post-subduction, extensional
Tectonic setting example		Qian'echong (Yang et al. 2013b); Jingduicheng (Yang et al. 2009)	Climax (Hall et al. 1974) Henderson (Seedorff and Einaudi 2004a, b; Wallace et al. 1978) Urad (Wallace et al. 1978) Questa (Cline and Bodnar 1994; Klemm et al. 2008)

area, as fully addressed in previous studies (Li et al. 2001; Mao et al. 2011; Pirajno 2013; and references therein).

Comparison with Climax-type Mo deposits

Climax-type porphyry molybdenum deposits document thirteen deposits that are found in a single region, the continental interior of western North America. All the deposits except Ruby Creek, British Columbia, were formed during extension subsequent to cessation of subduction of the Kula and Farallon plates beneath western North America (Ludington and Plumlee 2009). These deposits are high grade, rift related, fluorine-rich, and associated with alkali–calcic intrusions. The Yaochong deposit is located in a continental collision orogen and was formed by granitic magmatism associated with continental collision. The high contents of fluorine in the fluids and extensional environment of tectonic setting at Yaochong suggest an affinity with Climax-type deposits, whereas Mo grade is much lower at Yaochong and other porphyry Mo systems in the Qinling–Dabie orogen.

In Climax-type deposits, the earliest fluids were single-phase, CO_2-bearing aqueous fluids, were of low salinity and intermediate density, and were released from the evolving magma from mid-crustal to lower crustal level; by decompression from near-lithostatic to near-hydrostatic conditions, they boiled off a vapor phase, leaving behind a residual brine that ponded in the roof region of the granite porphyry; Mo precipitated from a dense, residual and probably sulfide-depleted brine, in response to cooling of the saline liquid from 420 °C to 350 °C (Klemm et al. 2008). By contrast, the Yaochong porphyry Mo system was formed with a large number of PC- and C-type inclusions in the minerals in earlier stages (Table 4). This unusual high CO_2 concentration of the fluids may hint a much earlier fluid exsolution (Li et al. 2012c), considering the lower solubility of CO_2 than H_2O and Cl in the melt. The S-type FIs identified at the Yaochong deposit usually contain chalcopyrite and/or transparent minerals such as calcite, but do not contain halite, unlike the extreme boiling-induced Mo enrichment and high salinity in the S-type inclusions in Climax-type deposits. At Yaochong deposit, strong potassic alteration is widely observed, but phyllic and propylitic alterations, which are extensively developed at Climax-type deposits (Ludington and Plumlee 2009), are relatively weak. This alteration feature is shared by all the Mesozoic porphyry Mo systems in the East Qinling and Dabie Shan, such as the deposits at Yuchiling (Li et al. 2012c), Jinduicheng (Yang et al. 2009), Nannihu (Yang et al. 2012), Tangjiaping (Chen and Wang 2011), and Qian'echong (Yang et al. 2013b).

Concluding remarks

1. The Yaochong Mo deposit is a porphyry mineral system in Dabie Shan. The hydrothermal mineralization includes four stages, namely stage 1 barren quartz + K-feldspar ± pyrite ± magnetite veins, stage 2 quartz + K-feldspar + molybdenite ± pyrite veins, stage 3 quartz + polymetallic sulfide veins, and stage 4 barren quartz ± carbonate ± fluorite veins. Mo mineralization mainly occurred in stages 2 and 3.
2. Pure CO_2 (PC-type), CO_2-bearing (C-type), aqueous (W-type), and solid-bearing (S-type) fluid inclusions were observed in hydrothermal minerals (quartz and fluorite). From early to late, the proportions of PC- and C-type fluid inclusions gradually decrease, whereas W-type inclusions become more prevalent. In late quartz ± carbonate ± fluorite veins, only W-type FIs are present.
3. As evidenced by the occurrence, microthermometric data and estimated minimum trapping pressures of fluid inclusions, as well as the H–O–C isotope systematics, the ore-forming fluids were initially high temperature, high pressure, relatively high salinity, and compositionally CO_2-rich and NaCl-poor and then gradually evolved to low-temperature, low-pressure, CO_2-poor, and low-salinity fluids. This change was related to fluid boiling and CO_2 escape, causing deposition of Mo and other sulfides.
4. The fluids forming the Yaochong porphyry Mo deposit were CO_2-rich but NaCl-poor, which is typical of continental collision setting, instead of volcanic arcs related to oceanic subduction.

Acknowledgments The research was supported by funds from the National 973-Program (Projects 2006CB403508 and 2012CB406602) and NSFC (Nos. 41203029 and 40730421). Field work was supported by No. 3 Regional Geological Survey Team of Henan Province and the Henan Bureau of Geological Exploration for Non-Ferrous Metals. Professor Li-Juan Wang and Dr. Nuo Li are thanked for their assistance with analytical work.

References

Ames L, Tilton GR, Zhou G (1993) Timing of collision of the Sino-Korean and Yangtze Cratons: U–Pb zircon dating of coesite-bearing eclogites. Geology 21:239–342

Bodnar RJ (1993) Revised equation and table for determining the freezing point depression of H_2O–NaCl solutions. Geochim Cosmochim Acta 57:683–684

Bodnar RJ (1995) Fluid inclusion evidence for a magmatic source for metals in porphyry copper deposits. Miner Assoc Can Short Course Ser 23:139–152

Bowers TS, Helgeson HC (1983) Calculation of the thermodynamic and geochemical consequences of nonideal mixing in the system H_2O–CO_2–NaCl on phase relations in geologic systems: equation of state for H_2O–CO_2–NaCl fluids at high pressures and temperatures. Geochim Cosmochim Acta 47:1247–1275

Brown PE (1989) Flincor: a microcomputer program for the reduction and investigation of fluid-inclusion data. Am Miner 74:1390–1393

Bryant DL, Ayers JC, Gao S, Miller CF, Zhang HF (2004) Geochemical, age, and isotopic constraints on the location of the Sino-Korean/Yangtze Suture and evolution of the Northern Dabie Complex, east central China. Geol Soc Am Bull 116(5–6):698–717

Carten RB, White WH, Stein HJ (1993) High-grade granite-related molybdenum systems: classification and origin. Geol Assoc Can Spec Pap 40:521–554

Chavagnac V, Jahn BM (1996) Coesite-bearing eclogites from the Bixiling Complex, Dabie Mountains, China: Sm–Nd ages, geochemical characteristics and tectonic implications. Chem Geol 133:29–51

Chen YJ (2013) The development of continental collision metallogeny and its application. Acta Petrol Sin 29:1–17 (in Chinese with English abstract)

Chen YJ, Fu SG (1992) Gold Mineralization in West Henan, China. China Seismological Press, Beijing (in Chinese with English abstract)

Chen YJ, Li N (2009) Diagnostic fluid inclusion and wallrock alteration of intrusion-related hypothermal ore-systems (porphyry, skarn, breccia pipe, vein and IOCG) formed in intercontinental settings: origin and difference from those in volcanic arc. Acta Petrol Sin 25:2477–2508 (in Chinese with English abstract)

Chen YJ, Wang Y (2011) Fluid inclusion study of the Tangjiaping Mo deposit, Dabie Shan, Henan Province: implications for the nature of porphyry systems of post-collisional tectonic settings. Int Geol Rev 53:635–655

Chen YJ, Li C, Zhang J, Li Z, Wang HH (2000) Sr and O isotopic characteristics of porphyries in the Qinling molybdenum deposit belt and their implication to genetic mechanism and type. Sci China Ser D 43(Suppl):82–94

Chen YJ, Chen HY, Zaw K, Pirajno F, Zhang ZJ (2007a) Geodynamic settings and tectonic model of skarn gold deposits in China: an overview. Ore Geol Rev 31:139–169

Chen YJ, Ni P, Fan HR, Pirajno F, Lai Y, Su WC, Zhang H (2007b) Diagnostic fluid inclusions of different types hydrothermal gold deposits. Acta Petrol Sin 23:2085–2108 (in Chinese with English abstract)

Chen YJ, Xiao WJ, Zhang JJ (2008) Ore-system as a geodynamic probe. Geol China 35:1059–1073 (in Chinese with English abstract)

Chen YJ, Zhai MG, Jiang SY (2009) Significant achievements and open issues in study of orogenesis and metallogenesis surrounding the North China continent. Acta Petrol Sin 25:2695–2726 (in Chinese with English abstract)

Chen YJ, Zhang C, Li N, Yang YF, Deng K (2012) Geology of the Mo deposits in Northeast China. J Jilin Univ (Earth Sci) 42:1223–1268 (in Chinese with English abstract)

Chen HJ, Chen YJ, Zhang J, Chen XZ, Zhang HD (2013) Zircon U–Pb ages and Hf isotope characteristics of the ore-bearing intrusion from the Shapinggou molybdenum deposit, Jinzhai County, Anhui Province. Acta Petrol Sin 29:131–145 (in Chinese with English abstract)

Clark KF (1972) Stockwork molybdenum deposits in western Cordillera of North America. Econ Geol 67:731–758

Clayton WM, Mayeda TK (1963) The use of bromine pentafluoride in the extraction of oxygen from oxides and silicates for isotopic analysis. Geochim Cosmochim Acta 27:43–52

Clayton RN, O'Neil JL, Mayeda TK (1972) Oxygen isotope exchange between quartz and water. J Geophys Res 77:3057–3067

Cline JS, Bodnar RJ (1991) Can economic porphyry copper mineralization be generated by a typical calc-alkaline melt? J Geophys Res 96:8113–8126

Cline JS, Bodnar RJ (1994) Direct evolution of brine from a crystallizing silicic melt at the Questa, New Mexico, molybdenum deposit. Econ Geol 89:1780–1802

Collins PLF (1979) Gas hydrates in CO_2-bearing fluid inclusions and the use of freezing data for estimation of salinity. Econ Geol 74:1435–1444

Diamond LW (1994) Introduction to phase relations of CO_2–H_2O fluid inclusions. In: De Vivo B, Frezzotti ML (eds) Fluid inclusions in minerals: methods and applications. Virginia Polytechnic Institute and State University, Blacksburg, VA, pp 131–158

Fan HR, Hu FF, Wilde SA, Yang KF, Jin CW (2011) The Qiyugou gold-bearing breccia pipes, Xiong'ershan region, central China: fluid inclusion and stable-isotope evidence for an origin from magmatic fluids. Int Geol Rev 53:25–45

Faure G (1986) Principles of isotope geology, 2nd edn. Wiley, New York, p 589

Friedman I (1953) Deuterium content of natural water and other substances. Geochim Cosmochim Acta 4:89–103

Fu B, Zheng YF, Xiao YL, Li YL, Gong B, Li SG, Sun WD, Zhang SQ, Zhang ZH (1998) Geochemical studies of eclogites and marbles from Sujiahe in the Western Dabie Mountains. Acta Geol Sin 72:323–339 (in Chinese with English abstract)

Graupner T, Kempe U, Dombon E, Patzold O, Leeder O, Spooner ETC (1999) Fluid regime and ore formation in the tungsten (-yttrium) deposits of Kyzyltau (Mongolie Altai): evidence for fluid variability in tungsten–tin ore systems. Chem Geol 154:21–58

Hacker BR, Ratschbacher LW, Ireland L (1998) U/Pb zircon ages constrain the architecture of the ultrahigh-pressure Qinling–Dabie orogen, China. Earth Planet Sci Lett 161:215–230

Hacker BR, Ratschbacher L, Webb L (2000) Exhumation of ultrahigh-pressure continental crust in east central China: late Triassic-early Jurassic tectonic unroofing. J Geophys Res 105(B6):13339–13364

Hall WE, Rriedman I, Nash JT (1974) Fluid inclusion and light stable isotope study of the climax molybdenum deposits, Colorado. Econ Geol 69:884–901

Henan Bureau of Geology and Mineral Resources (1989) The regional geology of Henan Province. Geological Publishing House, Beijing, pp 1–772 (in Chinese)

Hoefs J (1997) Stable isotope geochemistry, 4th edn. Springer, Berlin, p 201

Hu SX (1988) Geology and metallogeny of the collision belt between the north and the south China plates. Nanjing University Press, Nanjing, p 558 (in Chinese)

Jahn BM, Chen B (2007) Dabieshan UHP metamorphic terrane: Sr–Nd–Pb isotopic constraint to pre-metamorphic subduction polarity. Int Geol Rev 49:14–29

Jahn BM, Wu FY, Lo CH, Tsai CH (1999) Crust-mantle interaction induced by deep subduction of the continental crust: geochemical and Sr–Nd isotopic evidence from post-collisional mafic-ultramafic intrusions of the northern Dabie complex, central China. Chem Geol 157:119–146

Klemm LM, Pettke T, Heinrich CA, Campos E (2007) Hydrothermal evolution of the El Teniente deposit, Chile: porphyry Cu–Mo ore deposition from low-salinity magmatic fluids. Econ Geol 102:1021–1025

Klemm LM, Pettke T, Heinrich CA (2008) Fluid and source magma evolution of the Questa porphyry Mo deposit, New Mexico, USA. Miner Depos 43:533–552

Li C, Chen YJ, He SD (2001) East Qinling–Dabieshan lithosphere delaminating age, mechanism and direction-petrological evidences and stipulation. Chin J Geochem 20:59–72

Li N, Chen YJ, Zhang H, Zhao TP, Deng XH, Wang Y, Ni ZY (2007) Molybdenum deposits in East Qinling. Earth Sci Front 14:186–198 (in Chinese with English abstract)

Li HC, Xu ZW, Lu XC, Wang XD, Chen W, Zhai DX (2010) Study on fluid inclusion of the Dayinjian Mo deposit in Xinxian County, Henan Province, China. Geol J China Univ 16:236–246 (in Chinese with English abstract)

Li N, Carranza EJM, Ni ZY, Guo DS (2012a) The CO_2-rich magmatic-hydrothermal fluid of the Qiyugou breccia pipe, Henan Province, China: implication for breccia genesis and gold mineralization. Geochem: Explor Environ, Anal 12:147–160

Li N, Chen YJ, Ulrich T, Lai Y (2012b) Fluid inclusion study of the Wunugetu Cu–Mo deposit, Inner Mongolia, China. Miner Depos 47:467–482

Li N, Ulrich T, Chen YJ, Thompson TB, Peace V, Pirajno F (2012c) Fluid evolution of the Yuchiling porphyry Mo deposit, East Qinling, China. Ore Geol Rev 48:442–459

Li N, Chen YJ, Pirajno F, Ni ZY, Sun YL (2013a) Timing of the Yuchiling giant porphyry Mo system, eastern Qinling, central China, and implications for ore genesis. Miner Depos 48:505–524

Li Y, Li N, Yang YF, Wang P, Mei M, Zhang J, Chen HJ, Chen YJ (2013b) Geological features and geodynamic settings of the Mo deposits in the north segment of the Dabie Mountains. Acta Petrol Sin 29:95–106 (in Chinese with English abstract)

Lickfold V, Cook DR, Smith SG, Ulrich TD (2003) Endeavor copper-gold porphyry deposits, Northparkes, New South Wales: intrusive history and fluid evolution. Econ Geol 98:1607–1636

Linnen RL, William-Jones AE (1990) Evolution of aqueous-carbonic fluids during contact metamorphism, wall-rock alteration, and molybdenite deposition at Trout Lake, British Columbia. Econ Geol 85:1840–1856

Liu XC, Jahn BM, Liu DY, Dong SW, Li SZ (2004) SHRIMP U-Pb zircon dating of a metagabbro and eclogites from western Dabieshan (Hong'an Block), China, and its tectonic implications. Tectonophysics 394:171–192

Liu XC, Jahn BM, Dong SW, Lou YX, Cui JJ (2008) High-pressure metamorphic rocks from Tongbaishan, central China: U–Pb and $^{40}Ar/^{39}Ar$ age constraints on the provenance of protoliths and timing of metamorphism. Lithos 105:301–318

Liu XC, Jahn BM, Li SZ, Liu YS (2013) U–Pb zircon age and geochemical constraints on tectonic evolution of the Paleozoic accretionary orogenic system in the Tongbai orogen, central China. Tectonophysics 599:67–88

Lu HZ, Fan HR, Ni P, Ou GX, Shen K, Zhang WH (2004) Fluid inclusion. Science Press, Beijing (in Chinese)

Ludington S, Plumlee GS (2009) Climax-type porphyry molybdenum deposits. U.S. Geological Survey open file report 2009-1215, p 16

Mao JW, Xie GQ, Bierlein F, Qü WJ, Du AD, Ye HS, Pirajno F, Li HM, Guo BJ, Li YF, Yang ZQ (2008) Tectonic implications from Re–Os dating of Mesozoic molybdenum deposits in East Qinling–Dabie orogenic belt. Geochim Cosmochim Acta 72:4607–4626

Mao JW, Pirajno F, Xiang JF, Gao JJ, Ye HS, Li YF, Guo BJ (2011) Mesozoic molybdenum deposits in the east Qinling–Dabie orogenic belt: characteristics and tectonic settings. Ore Geol Rev 43:264–293

Masterman GJ, Cooke DR, Berry RF, Lee AW, Clark AH (2005) Fluid chemistry, structural setting and emplacement history of the Rosario Cu–Mo porphyry and Cu–Ag–Au epithermal veins, Collahuasi district, northern Chile. Econ Geol 100:835–862

McCoy D, Newberry RJ, Layer P, DiMarchi JJ, Bakke A, Masterman S, Minehane DL (1997) Plutonic-related gold deposits of Interior Alaska. In: Goldfarb RJ, Miller LD (eds) Mineral deposits of Alaska. Econ Geol Mon 9:191–241

Meng S, Yan C, Lai Y, Shu QH, Sun Y (2013) Study on the mineralization chronology and characteristics of mineralization fluid from the Chehugou porphyry Mo–Cu deposit, Inner Mongolia. Acta Petrol Sin 29: 255–269 (in Chinese with English abstract)

Mernagh TP, Bastrakov EN, Zaw K, Wygralak AS, Wyborn LA (2007) Comparison of fluid inclusion data and mineralization processes for Australian orogenic gold and intrusion-related gold systems. Acta Petrol Sin 23:21–32

Mirsa KC (2000) Understanding mineral deposits. Kluwer Academic Publishers, Dordrecht, pp 353–413

Mutschler FE, Wright EG, Ludington S, Abbott JT (1981) Granite molybdenite systems. Econ Geol 76:874–897

Nash JT (1976) Fluid inclusion petrology data from porphyry copper deposits and application to exploration. US Geological Survey professional paper 907-D, pp 1–16

Phillips GN, Zhou T (1999) Gold-only deposits and Archean granite. SEG Newslett 37:6

Pirajno F (2009) Hydrothermal processes and mineral systems. Springer, Berlin, p 1250

Pirajno F (2013) The geology and tectonic settings of China's mineral deposits. Springer, Berlin, p 679

Richards JP (2003) Tectono-magmatic precursors for porphyry Cu–(Mo–Au) deposit formation. Econ Geol 98:1515–1533

Richards JP (2009) Postsubduction porphyry Cu–Au and epithermal Au deposits: products of remelting of subduction-modified lithosphere. Geology 37:247–250

Roedder E (1984) Fluid inclusions. Rev Miner 12:646

Rumble D, Wang QC, Zhang RY (2000) Stable isotope geochemistry of marbles from the coesite UHP terrains of Dabieshan and Sulu, China. Lithos 52:79–95

Schidlowski M (1998) Beginning of terrestrial life: problems of the early record and implications for extraterrestrial scenarios. Inst Methods Missions Astrobiol SPIE 3441:149–157

Seedorff E, Einaudi M (2004a) Henderson porphyry molybdenum system, Colorado: I. Sequence, abundance of hydrothermal mineral assemblages, flow paths of evolving fluids, evolutionary style. Econ Geol 99:3–37

Seedorff E, Einaudi M (2004b) Henderson porphyry molybdenum system, Colorado: II. Decoupling of introduction, deposition of metals during geochemical evolution of hydrothermal fluids. Econ Geol 99:39–72

Seedorff E, Dilles JH, Proffett JM, Einaudi MT, Zurcher L, Stavast WJA, Johnson DA, Barton MD (2005) Porphyry deposit: characteristics and origin of hypogene features. Econ Geol 100:251–298

Sillitoe RH (1972) A plate tectonic model for the origin of porphyry copper deposits. Econ Geol 67:184–197

Sillitoe RH (1980) Types of porphyry molybdenum deposits. Min Mag 142(550–551):553

Spiridinov EM (1996) Granitic rocks and gold mineralization of North Kazakhstan. In: Shatov V, Seltmann R, Kremenetsky A, Lehmann B, Popov V, Ermolov P (eds) Granite-related ore deposits of central Kazakhstan and adjacent areas. Glagol Publishing House, St Petersburg, pp 197–217

Suo ST, Zhong ZQ, You Z (2000) Extensional deformation of post ultrahigh-pressure metamorphism and exhumation process of ultrahigh-pressure metamorphic rocks in the Dabie massif, China. Sci China Ser D 43:225–236

Tang HS, Chen YJ, Wu G, Lai Y (2008) The C–O isotope composition of the Liaohe Group, northern Liaoning province and its geologic implications. Acta Petrol Sin 24:129–138 (in Chinese with English abstract)

Tang HS, Wu G, Lai Y (2009) The C–O isotope geochemistry and genesis of the Dashiqiao magnesite deposit, Liaoning province, NE China. Acta Petrol Sin 25:455–467

Tang HS, Chen YJ, Wu G, Lai Y (2011) Paleoproterozoic positive $\delta^{13}C_{carb}$ excursion in the northeastern Sinokorean craton: evidence of the Lomagundi event. Gondwana Res 19:471–481

Tang HS, Chen YJ, Santosh M, Zhong H, Wu G, Lai Y (2013) C–O isotope geochemistry of the Dashiqiao magnesite belt, North China Craton: implications for the Great Oxidation Event and ore genesis. Geol J 48:467–483

Ulrich T, Heinrich CA (2001) Geology and alteration geochemistry of the porphyry Cu–Au deposit at Bajo de la Alumbrera Argentina. Econ Geol 96:1719–1742

Ulrich T, Günther D, Heinrich CA (1999) Au concentrations of magmatic brines and the metal budget of porphyry copper deposits. Nature 399:676–679

Wallace SR, MacKenzie WB, Blair RG, Muncaster NK (1978) Geology of the Urad and Henderson molybdenite deposits, Clear Creek County, Colorado, with a section on a comparison of these deposits with those at Climax, Colorado. Econ Geol 73:325–368

Wang XM, Liou JG, Mao HK (1989) Coesite-bearing eclogite from the Dabie Mountains in central China. Geology 17:1085–1088

Wang Y, Chen YJ, Ma HW, Xu YL (2009) Study on ore geology and fluid inclusions of the Tangjiaping Mo deposit, Shangcheng County, Henan Province. Acta Petrol Sin 25:468–480 (in Chinese with English abstract)

Wang P, Yang YF, Mei M, Li ZL, Wang LJ (2013) Fluid evolution of the Yaochong porphyry Mo deposit, Xinxian county, Henan province, China. Acta Petrol Sin 29:107–120 (in Chinese with English abstract)

Westra G, Keith SB (1981) Classification and genesis of stockwork molybdenum deposits. Econ Geol 76:844–873

Woodcock JR, Hollister VF (1978) Porphyry molybdenite deposits of the North American Cordillera. Miner Sci Eng 10:3–18

Wu YS, Xiang N, Tang HS, Zhou KF, Yang YF (2013) Molybdenite Re–Os isotope age of the Donggebi Mo deposit and the Indosinian metallogenic event in eastern Tianshan. Acta Petrol Sin 29:121–130 (in Chinese with English abstract)

Xiang N, Yang YF, Wu YS, Zhou KF (2013) Fluid inclusion study of the Baishan porphyry Mo deposit in the Eastern Tianshan ore field, Xinjiang Province. Acta Petrol Sin 29:146–158 (in Chinese with English abstract)

Xiao WJ, Windley BF, Huang BC, Han CM, Yuan C, Chen HL, Sun M, Sun S, Li JL (2009) End-Permian to mid-Triassic termination of the accretionary processes of the southern Altaids: implications for the geodynamic evolution, Phanerozoic continental growth, and metallogeny. Int J Earth Sci 98:1189–1217

Xu ST, Okay AI, Ji S, Sengor AMC, Su W, Liu Y, Jiang L (1992) Diamond from the Dabie Shan metamorphic rocks and its implication for tectonic setting. Science 256:80–82

Xu HJ, Ma CQ, Kai Y (2007) Early cretaceous granitoids and their implications for the collapse of the Dabie orogen, eastern China: SHRIMP zircon U–Pb dating and geochemistry. Chem Geol 240:238–259

Yang ZQ (2007) Re–Qs isotopic ages of Tangjiaping molybdenum deposit in Shangcheng County, Henan and their geological significance. Miner Dep 26:289–295 (in Chinese with English abstract)

Yang Y, Zhang J, Lu YH, Liu JJ, Sun YL, Li J, Yang ZQ (2008) Hydrothermal metallogeny of the Tangjiaping molybdenum deposit, Henan Provinces. Geol China 35:1240–1249 (in Chinese with English abstract)

Yang YF, Li N, Ni ZY (2009) Fluid inclusion study of the Jinduicheng porphyry Mo deposit, Hua County, Shanxi Province. Acta Petrol Sin 25:2983–2994 (in Chinese with English abstract)

Yang YF, Li N, Chen YJ (2012) Fluid inclusion study of the Nannihu giant porphyry Mo-W deposit, Henan Province, China: implications for the nature of porphyry ore-fluid systems formed in a continental collision setting. Ore Geol Rev 46:83–94

Yang Y, Chen YJ, Zhang J, Zhang C (2013a) Ore geology, fluid inclusions and four-stage hydrothermal mineralization of the Shangfanggou giant Mo–Fe deposit in Eastern Qinling, central China. Ore Geol Rev 55:146–161

Yang YF, Chen YJ, Li N, Mi M, Xu YL, Li FL, Wan SQ (2013b) Fluid inclusion and isotope geochemistry of the Qian'echong giant porphyry Mo deposit, Dabie Shan, China: a case of NaCl-poor, CO_2-rich fluid systems. J Geochem Explor 124:1–13

Ye BD, Jian P, Xu J, Cui F, Li Z, Zhang Z (1993) The Sujiahe terrance collage belt and its constitution and evolution along the northern hillslope of the Tongbai–Dabie orogenic belt. Press of China University of Geoscience, Wuhan, pp 1–81 (in Chinese with English abstract)

Yin HF, Yang FQ, Lai XL (1991) Late Hercynian–Indosinian tectonics and geography in Qinling. In: Ye LJ, Qian XL, Zhang GW (eds) Proceedings of symposium on Qinling Orogenic Belt. Northwest University Press, Xi'an, pp 68–77 (in Chinese)

Zeng QD, Liu JM, Zhang ZL, Chen WJ, Zhang WQ (2011) Geology and geochronology of the Xilamulun molybdenum metallogenic belt in eastern Inner Mongolia, China. Int J Earth Sci 100:1791–1809

Zeng QD, Liu JM, Qin KZ, Fan HR, Chu SX, Wang YB, Zhou LL (2013) Types, characteristics, and time–space distribution of molybdenum deposits in China. Int Geol Rev 55:1311–1358

Zhang LG (1989) Petrogenetic and minerogenetic theories and prospecting: stable isotopic geochemistry of main type ore deposits and granitoids of China. Press of Beijing University of Technology, Beijing, p 200 (in Chinese with English abstract)

Zhang J, Chen YJ, Yang Y, Deng J (2011a) Lead isotope systematics of the Weishancheng Au–Ag belt, Tongbai Mountains, central China: implication for ore genesis. Int Geol Rev 53: 656–676

Zhang ZW, Yang XY, Dong Y, Zhu BQ, Chen DF (2011b) Molybdenum deposits in the eastern Qinling, central China: constraints on the geodynamics. Int Geol Rev 53:261–290

Zhang C, Li N, Chen YJ, Zhao XC (2013a) Zircon U–Pb ages and Hf isotopic compositions of the intrusive rocks in the Xing'a Mo–Cu deposit, Inner Mongolia. Acta Petrol Sin 29:217–230 (in Chinese with English abstract)

Zhang J, Chen YJ, Pirajno F, Deng J, Chen HY (2013b) Geology, isotope systematics and ore genesis of the Yindongpo gold deposit, Tongbai Mountains, central China. Ore Geol Rev 53:343–356

Zhao ZF, Zheng YF, Wei CS, Wu YB (2007) Post-collisional granitoids from the Dabie orogen in China: zircon U–Pb age, element and O isotope evidence for recycling of subducted continental crust. Lithos 93:248–272

Zheng YF, Fu B, Gong B, Wang ZR (1998) Carbon isotope anomaly in marbles associated with eclogites from the Dabie Mountains in China. J Geol 106:97–104

Zheng YF, Wu YB, Zhao ZF, Zhang SB, Xu P, Wu FY (2005) Metamorphic effect on zircon Lu–Hf and U–Pb isotope systems in ultrahigh-pressure eclogite-facies metagranite and metabasite. Earth Planet Sci Lett 240:378–400

Zheng YF, Zhao ZF, Wu YB, Zhang SB, Liu XM, Wu FY (2006) Zircon U–Pb age, Hf and O isotope constraints on protolith origin of ultrahigh-pressure eclogite and gneiss in the Dabie orogen. Chem Geol 231:135–158

Zhong ZQ, Suo ST, You Z (1999) Regional-scale extensional tectonic pattern of ultrahigh-P and high-P metamorphic belts from the Dabie massif, China. Int Geol Rev 41:1033–1041